ARTICLE IN PRESS

Available online at www.sciencedirect.com

ScienceDirect

Comput. Methods Appl. Mech. Engrg. ▮ (▮▮▮▮) ▮▮▮–▮▮▮

Computer methods in applied mechanics and engineering

www.elsevier.com/locate/cma

Patient-specific modeling for left ventricular mechanics using data-driven boundary energies

L. Asner[a,1], M. Hadjicharalambous[a,1], R. Chabiniok[c,a], D. Peressutti[a], E. Sammut[a], J. Wong[a], G. Carr-White[d,a], R. Razavi[b], A.P. King[a], N. Smith[e,a], J. Lee[a], D. Nordsletten[a,*]

[a] *Department of Biomedical Engineering, King's College London, UK*
[b] *Division of Imaging Sciences and Biomedical Engineering, King's College London, UK*
[c] *Inria and Paris-Saclay University, Palaiseau, France*
[d] *Department of Cardiology, Guy's and St Thomas' NHS Foundation Trust, London, UK*
[e] *Faculty of Engineering, University of Auckland, Auckland, New Zealand*

Highlights

- Development of boundary conditions using patient-specific data.
- A systematic analysis of cardiac mechanics boundary conditions.
- Demonstration of efficacy for 6 patient-specific models.
- Novel quantitative comparison with non-invasive imaging data.

Abstract

Supported by the wide range of available medical data available, cardiac biomechanical modeling has exhibited significant potential to improve our understanding of heart function and to assisting in patient diagnosis and treatment. A critical step towards the development of accurate patient-specific models is the deployment of boundary conditions capable of integrating data into the model to enhance model fidelity. This step is often hindered by sparse or noisy data that, if applied directly, can introduce non-physiological forces and artifacts into the model. To address these issues, in this paper we propose novel boundary conditions which aim to balance the accurate use of data with physiological boundary forces and model outcomes through the use of data-derived boundary energies. The introduced techniques employ Lagrange multipliers, penalty methods and moment-based constraints to achieve robustness to data of varying quality and quantity. The proposed methods are compared with commonly used boundary conditions over an idealized left ventricle as well as over *in vivo* models, exhibiting significant improvement in model accuracy. The boundary conditions are also employed in *in vivo* full-cycle models of healthy and diseased hearts, demonstrating the ability of

* Correspondence to: 3FL Lambeth Wing, St Thomas Hospital, Westminster Bridge Rd, London SE1 7EH, UK.
E-mail address: david.nordsletten@gmail.com (D. Nordsletten).

[1] Authors acknowledge joint first authorship.

http://dx.doi.org/10.1016/j.cma.2016.08.002

the proposed approaches to reproduce data-derived deformation and physiological boundary forces over a varied range of cardiac function.

Keywords: Cardiac mechanic; Patient-specific modeling; Patient-specific boundary conditions; Finite element method; Medical imaging

1. Introduction

Diagnostic medicine, medical imaging and novel therapies have rapidly improved patient outcomes across a wide range of heart conditions. While this has led to substantial progress, challenges in understanding (patho)physiology, improving patient diagnosis and therapy planning and designing the next generation of devices remain. Cardiac biomechanics provides a powerful tool for evaluating and predicting the complex behaviors of the heart and is increasingly playing an important role in translating physiologically based models towards strategies for understanding and treating heart failure [1–3]. A critical step in this effort is the ability to devise high fidelity computational biomechanical models that are capable of replicating cardiac function on a patient-by-patient basis.

Bolstered by continual improvements in cardiac biorheology, medical imaging and computational techniques, it is now possible to create high fidelity biophysical heart models [4–10]. Early studies in animal heart muscle [11–13] and more recent studies of human tissue [14] have enabled development of constitutive laws characterizing the anisotropic material behavior of the myocardium. Moving these excised tissue results into computational models was facilitated by descriptions of the laminar muscle structure, first determined from anatomical dissections [15] and more recently by diffusion tensor imaging [16,17]. Utilizing biomechanical models in the human heart has been enabled by medical imaging, capable of describing *in vivo* anatomy [18], detailed motion [19], blood flow [20] and even non-invasive estimates of pressure [21–23]. Exploitation of these patient data sources has been achieved through novel advancements in data assimilation [24,25,5] and parameter estimation techniques [10,26].

An important step towards translating biophysical heart models on a patient-by-patient basis is the personalization of cardiac function based on available data. A key challenge in this effort is the determination and handling of boundary conditions. Despite the importance of these conditions for correctly simulating the biomechanics of the heart, these effects are often less well-studied. Typical imaging – such as CINE or tagged MRI – can provide some guidance on motion [27,28]; however, this characterization can be incomplete or corrupted by noise. Use of this type of data also requires segmentation and image processing techniques that, in themselves, can introduce inaccuracies. Exploiting this data to drive computational biomechanical models in a manner which maintains model fidelity and minimizes modeling errors remains an open and important challenge.

Here we propose to address this issue by augmenting the traditional elastic energy potential minimization problem (commonly applied for cardiac biomechanics simulation) with a series of novel data-driven boundary energy terms. In this paper we focus on the isolated left ventricle (LV) (see Fig. 1)—commonly used in studies of cardiac biomechanics [29–32]. While lacking connection to other cardiac chambers, isolated LV models are often more straightforward to segment and characterize from medical imaging data, particularly MRI and ECHO. In addition, the LV is often the focus of heart failure studies due to the functional significance of its failure. Addressing boundary conditions on the LV, we develop tailored energy terms for each boundary component, focusing on the use of data available from non-invasive medical imaging. Through use of Lagrange multipliers, penalty variables and moment-based constraints, we devise terms which balance the use of real data with the energy required to force data-derived motion onto the computational model. These introduced techniques are then systematically compared with other common boundary conditions, highlighting their influence on simulation results as well as the benefits of the proposed approaches. Comparisons were carried out using an idealized LV mechanics model as well as patient-specific LV mechanics models based on data from 3 patients with dilated cardiomyopathy (DCM) as well as 3 volunteers. Efficacy of the proposed approach is demonstrated through direct quantitative comparisons between 3D displacement fields extracted from medical imaging data and simulation results.

The remainder of this paper is outlined as follows. A brief review of the LV cardiac mechanics model used is provided in Section 2. A summary of the elastic energy potential minimization approach is then presented in Section 3, followed by a description of the novel boundary energy potentials. An overview of the finite element implementation is

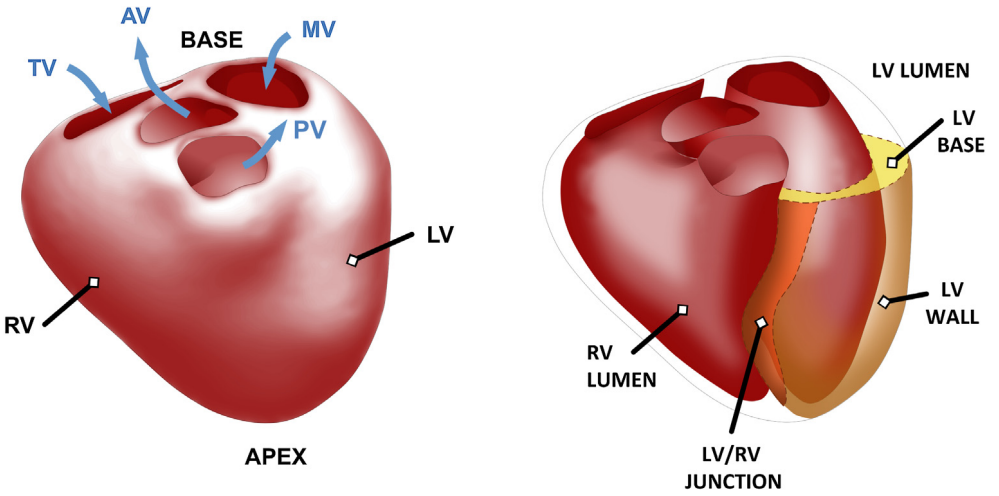

Fig. 1. (Left) Illustration of the biventricular heart and major inlet/outlet valves and (Right) the portion of the left ventricle considered in LV model analysis. Abbreviations: AV = aortic valve, LV = left ventricle, MV = mitral valve, PV = pulmonary valve, RV = right ventricle, TV = tricuspid valve.

subsequently provided in Section 4, followed by a description of both idealized and patient-specific models developed in this work (Section 5). Sections 6–8 systematically assess each boundary energy potential term and, where possible, compare with other common approaches. The proposed model is then applied to three patient and three volunteer datasets, illustrating model accuracy as well as the efficacy of the proposed approach (Section 9). The paper concludes with a summary of the results, key outcomes and future directions (Section 10).

2. Cardiac mechanics

In this section we briefly outline the basic components for the LV cardiac mechanics model used in this work. Under zero loading conditions, the muscular wall of the LV (or myocardium) is characterized by the reference domain $\Omega_0 \subset \mathbb{R}^3$ (with reference coordinates $\mathbf{X}$). The LV only model results from truncation of the heart below the valves in a short axis plane (see Figs. 1 and 2). The boundary of Ω_0 is subdivided into three distinct surfaces: the base Γ_0^b, the endocardium Γ_0^l and the epicardium Γ_0^e. For each boundary, we use $\boldsymbol{N}$ to denote the outward-facing normal vector. As we will track the motion of the base plane, we use $\boldsymbol{N}_b$ to denote the mean unit normal vector on Γ_0^b and define a local coordinate system with orthonormal basis vectors $\{\boldsymbol{N}_1, \boldsymbol{N}_2, \boldsymbol{N}_b\}$ (see Fig. 2). As the heart deforms, we use lower case $\{\mathbf{n}_1, \mathbf{n}_2, \mathbf{n}_b\}$ to denote the deformed orientations. Throughout the cardiac cycle, at each time $t \in (0, T], \ T > 0$, the deformed physical domain is denoted by $\Omega(t) \subset \mathbb{R}^3$ (with physical coordinates $\boldsymbol{x}$) with boundaries Γ^k and respective normals $\boldsymbol{n}$. We assume that for every $t \in (0, T]$ the mapping between $\boldsymbol{x}$ and $\mathbf{X}$ is bijective.

In order to represent the highly anisotropic behavior given by the laminar structure of the myocardium, we define fiber directions $\boldsymbol{f}_0$ over Ω_0 (see Fig. 2). While new techniques provide the potential to gain some insight into the structure of these fibers on a patient-by-patient basis [33,17,34], in the absence of personalized data, we prescribe an idealized distribution. Briefly, a Laplacian problem was solved on the domain Ω_0 to make a harmonic extension of the endocardial to epicardial surface normal vectors (radial/sheet direction). Subsequently, at each point, fibers were defined in the sheet direction plane. The fiber vector was defined based on its angle about the sheet axis, with an angle of 0° indicating vectors oriented in the circumferential clock-wise direction (when viewed from the base) and an angle of 90° indicating vectors oriented in the long-axis direction. A linear distribution in angle was defined transmurally, with the angle varying between 60° at the endocardium and −60° at the epicardium [35,36] (see Fig. 2).

In modeling cardiac mechanics we seek to find the deformation $\boldsymbol{u} = \boldsymbol{x} - \boldsymbol{X}$ and the hydrostatic pressure p on $\Omega_0 \times (0, T]$. As we outline in the subsequent section, these variables can be found by minimizing an elastic energy potential. For this, we must model the internal energy within the tissue due to deformation using a strain energy potential ψ. In this paper, we treat the myocardium as an incompressible, hyperelastic material with the distortional strain energy $\psi = \psi_p + \psi_a$ comprised of passive and active parts. In this work we use the reduced Holzapfel–Ogden

Please cite this article in press as: L. Asner, et al., Patient-specific modeling for left ventricular mechanics using data-driven boundary energies, Comput. Methods Appl. Mech. Engrg. (2016), http://dx.doi.org/10.1016/j.cma.2016.08.002

model [13] to describe the passive behavior of the myocardium using

$$\psi_p(\boldsymbol{F_u}) = \frac{a}{2b}\left\{\exp(b[\mathrm{II}_{\boldsymbol{F}} - 3]) - 1\right\} + \frac{a_f}{2b_f}\left\{\exp(b_f[\mathrm{II}_{\boldsymbol{F},f} - 1]^2) - 1\right\}, \tag{1}$$

which combines good model fidelity and parameter identifiability [37]. Here we have used some basic kinematic quantities: $\mathrm{II}_{\boldsymbol{F},f} = |\boldsymbol{F_u}\boldsymbol{f}_0|^2$ and $\mathrm{II}_{\boldsymbol{F}} = \boldsymbol{F_u} : \boldsymbol{F_u}$ denoting material invariants, $\boldsymbol{F_u} = \nabla_{\boldsymbol{X}}\boldsymbol{u} + \boldsymbol{I}$ the deformation gradient tensor and $J_{\boldsymbol{u}} = \det(\boldsymbol{F_u})$ its determinant. Here a, a_f, b and b_f are material parameters. a characterizes the bulk stiffness of the myocardium while a_f describes the stiffness in the direction of fibers $\boldsymbol{f}_0$. Similarly, the parameters b and b_f characterize the shape of the nonlinear response in bulk and the fiber direction.

A simple length-dependent active constitutive law [10] is used in the model, where activation occurs along the fibers, and a single patient-specific active tension $\alpha(t)$ is applied across the domain at any given time $t \in (0, T]$. The structure of the idealized fiber distribution results in a singularity arising in the apical region, causing spurious pressure peaks. As the microstructure in the human heart is less ordered near the apex, the active strain energy function is augmented with an isotropic term, and both components are scaled so that the total energy is fiber-oriented in most of the domain and isotropic at the apex, *i.e.*

$$\psi_a(\boldsymbol{F_u}, \mathbf{X}, t) = \alpha(t)\left\{[1 - D(\mathbf{X})]\int_0^{\mathrm{II}_{\boldsymbol{F},f}} g(\xi)\, d\xi \; + D(\mathbf{X})\int_0^{\mathrm{II}_{\boldsymbol{F}}} g(\xi/3)\, d\xi\right\}, \tag{2}$$

where

$$D(\mathbf{X}) = \exp\left[-(\|\mathbf{X} - \boldsymbol{X}_a\|/0.02L_{la})^2\right], \quad g(\xi) = \tanh\left(2[\sqrt{\xi} - l_0]\right).$$

Here $D(\mathbf{X})$ is a distance function taking the value 1 near the apex point $\mathbf{X}_a$ and rapidly decaying to zero (with L_{la} being the long-axis length and the factor 0.02 set so that $D(\mathbf{X}) < 0.05$ at a distance of $\sim 0.06L_{la}$), as illustrated in Fig. 3. g is a given activation function which provides length-dependent scaling of the active strain energy, with $l_0 = 0.8$ the lower bound for the myocyte compressive strain [38]. From the strain energy, we can derive the first Piola–Kirchhoff stress [39]

$$\begin{aligned}\boldsymbol{P_u} &= \sum_{k\in\{p,a\}}\left(\frac{\partial\psi_k}{\partial\mathrm{II}_{\boldsymbol{F}}}\frac{\partial\mathrm{II}_{\boldsymbol{F}}}{\partial\boldsymbol{F_u}} + \frac{\partial\psi_k}{\partial\mathrm{II}_{\boldsymbol{F},f}}\frac{\partial\mathrm{II}_{\boldsymbol{F},f}}{\partial\boldsymbol{F_u}}\right)\\ &= a\exp(b[\mathrm{II}_{\boldsymbol{F}} - 3])\boldsymbol{F_u} + 2a_f[\mathrm{II}_{\boldsymbol{F},f} - 1]\exp(b_f[\mathrm{II}_{\boldsymbol{F},f} - 1]^2)\boldsymbol{F_u}\boldsymbol{f}_0 \otimes \boldsymbol{f}_0\\ &\quad + \alpha(t)D(\mathbf{X})g(\mathrm{II}_{\boldsymbol{F}}/3)\boldsymbol{F_u} + \alpha(t)[1 - D(\mathbf{X})]g(\mathrm{II}_{\boldsymbol{F},f})\boldsymbol{F_u}\boldsymbol{f}_0 \otimes \boldsymbol{f}_0.\end{aligned} \tag{3}$$

Finally, in order to introduce some of the data-driven boundary conditions in the next section, we use the following notation: $\boldsymbol{u}_d(t)$ represents the displacements extracted from the data, e.g. as discussed in Section 5, and $V_{lv}(t)$ represents the volume of the left-ventricular cavity Ω_{lv} computed from $\boldsymbol{u}_d(t)$.

3. Elastic energy potential and weak form equations

The mechanics of the heart can be solved by finding the critical point of the total potential energy function Π_t (at some time $t \in (0, T]$), where the displacement and pressure state variables satisfy the saddle point condition [39],

$$\Pi_t(\boldsymbol{u}(t), p(t)) = \inf\{\sup\{\Pi_t(\boldsymbol{v}, q),\ q \in P\},\ \boldsymbol{v} \in \boldsymbol{U}\}. \tag{4}$$

In this approach, the saddle point problem is used to solve a quasi-static system, whereby the displacement and pressure are sought for each time point $t \in [0, T]$ throughout the cardiac cycle subject to varying boundary conditions or activation states. $\boldsymbol{U}$ and P denote the suitable function spaces for displacement and pressure variables, respectively, at each individual point in time (see Appendix A). The total potential energy $\Pi_t = \Pi_t^{int} + \Pi_t^{ext}$ is the sum of the internal (superscript int) and external (superscript ext) energy terms, with the internal energy given by

$$\Pi_t^{int}(\boldsymbol{v}, q) = \int_{\Omega_0} \psi(\boldsymbol{F_v}, \mathbf{X}, t) + q(J_{\boldsymbol{v}} - 1)\, d\boldsymbol{X}, \tag{5}$$

Please cite this article in press as: L. Asner, et al., Patient-specific modeling for left ventricular mechanics using data-driven boundary energies, Comput. Methods Appl. Mech. Engrg. (2016), http://dx.doi.org/10.1016/j.cma.2016.08.002

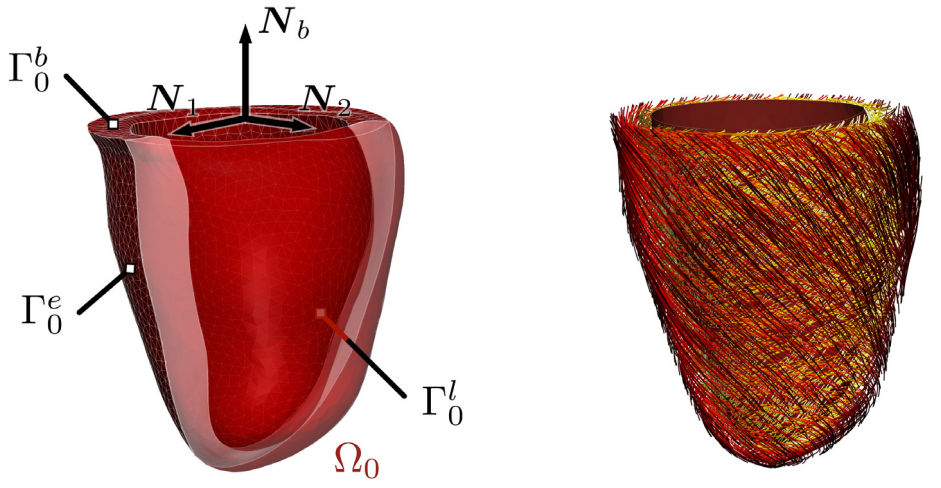

Fig. 2. (Left) Illustration of the left ventricle domain (Ω_0) and its constituent boundaries: base plane (Γ_0^b), endocardial (Γ_0^l), and epicardial (Γ_0^e). $\{\boldsymbol{N}_1, \boldsymbol{N}_2, \boldsymbol{N}_b\}$ denotes the orthonormal coordinate frame for tracking the base plane motion. (Right) Illustration of the fiber architecture in the left ventricle, showing streamlines in the fiber direction colored white (endocardial) to dark red (epicardial) based on the transmural location. (For interpretation of the references to color in this figure legend, the reader is referred to the web version of this article.)

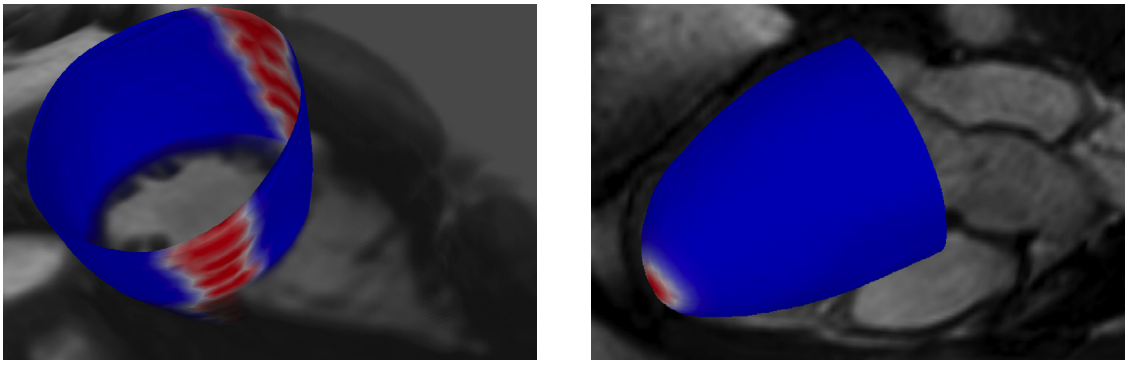

Fig. 3. (Left) Illustration of the function $H : \Gamma_0^e \to [0, 1]$ labeling the RV/LV junction on the epicardium and (Right) the apex distance function $D : \Omega_0 \to [0, 1]$ used to scale the orthotropic vs. isotropic terms in the active strain.

where $\psi(\boldsymbol{F}_v, \mathbf{X}, t) = \psi_p(\boldsymbol{F}_v) + \psi_a(\boldsymbol{F}_v, \mathbf{X}, t)$ is the strain energy potential defined in Eqs. (1) and (2) and the second term is used to enforce mass conservation. Within the LV, the external energy Π_t^{ext} can be conveniently partitioned over the base Γ_0^b, endocardial lumen Γ_0^l, and epicardial Γ_0^e (see Fig. 2). A variety of boundary conditions have been employed in models of the left ventricle, providing varying degrees of accuracy and introducing additional forces to the problem (as will be presented below). To examine the numerical and modeling implications of these conditions, in this paper we augment the problem in Eq. (4) by writing Π_t^{ext} as a sum of external boundary energies, *i.e.*

$$\Pi_t^{ext}(\boldsymbol{v}, \boldsymbol{\mu}) = \sum_{k \in \{b,l,e\}} \Pi_t^k(\boldsymbol{v}, \boldsymbol{\mu}_k) \tag{6}$$

with $\boldsymbol{\mu}$ denoting any additional variables $\{\boldsymbol{\mu}_k\}$ – tractions or pressures – defined over each boundary domain Γ_0^k, $k \in \{b, l, e\}$. The specifics of these variables depend on the employed boundary conditions and will be introduced throughout the remainder of this section. We may re-write the saddle-point problem in Eq. (4) as,

$$\Pi_t(\boldsymbol{u}(t), p(t), \boldsymbol{\lambda}(t)) = \inf \{\sup \{\Pi_t(\boldsymbol{v}, q, \boldsymbol{\mu}),\ (q, \boldsymbol{\mu}) \in P \times \boldsymbol{\Lambda}\},\ \boldsymbol{v} \in \boldsymbol{U}\} \tag{7}$$

where the the total potential energy $\Pi_t = \Pi_t^{int} + \Pi_t^{ext}$ is now a functional on $\boldsymbol{U} \times P \times \boldsymbol{\Lambda}$, $(\boldsymbol{u}, p, \boldsymbol{\lambda})$ are the state variables (*e.g.* unknown displacement, pressure and boundary tractions and/or pressures, respectively) and $(\boldsymbol{v}, q, \boldsymbol{\mu}) \in \boldsymbol{U} \times P \times \boldsymbol{\Lambda}$ arbitrary functions within the selected search space. As the saddle point problem is posed at each time point, in what

Please cite this article in press as: L. Asner, et al., Patient-specific modeling for left ventricular mechanics using data-driven boundary energies, Comput. Methods Appl. Mech. Engrg. (2016), http://dx.doi.org/10.1016/j.cma.2016.08.002

follows we simplify the notation such that $(\boldsymbol{u}, p, \boldsymbol{\lambda}) = (\boldsymbol{u}(t), p(t), \boldsymbol{\lambda}(t))$ unless the context is ambiguous. The solution $(\boldsymbol{u}, p, \boldsymbol{\lambda}) \in \boldsymbol{U} \times P \times \boldsymbol{\Lambda}$ is then the critical point of the functional satisfying

$$\mathcal{D}_{(\boldsymbol{u},p,\boldsymbol{\lambda})}\Pi_t(\boldsymbol{u}, p, \boldsymbol{\lambda})[\boldsymbol{v}, q, \boldsymbol{\mu}] = 0, \quad \forall\, (\boldsymbol{v}, q, \boldsymbol{\mu}) \in \boldsymbol{U} \times P \times \boldsymbol{\Lambda}, \tag{8}$$

with $\mathcal{D}_{(\boldsymbol{u},p,\boldsymbol{\lambda})}\Pi$ denoting the sum of directional derivatives $\mathcal{D}_{\boldsymbol{u}}\Pi$, $\mathcal{D}_p\Pi$ and $\mathcal{D}_{\boldsymbol{\lambda}}\Pi$ [39]. Eq. (8) results in a weak form statement of the solid mechanics problem and can be split into directional derivatives of internal and individual external boundary energy terms. With this approach in mind, we use $\mathcal{A}_t$ to denote the directional derivative of the internal energy potential (or equivalently, the nonlinear weak form operator) from Eq. (5), *i.e.*

$$\mathcal{A}_t(\boldsymbol{u}, p; \boldsymbol{v}, q) = \mathcal{D}_{(\boldsymbol{u},p)}\Pi_t^{int}(\boldsymbol{u}, p)[\boldsymbol{v}, q] = \int_{\Omega_0} (\boldsymbol{P}_{\boldsymbol{u}} + p J_{\boldsymbol{u}} \boldsymbol{F}_{\boldsymbol{u}}^{-T}) : \nabla_{\boldsymbol{X}} \boldsymbol{v} + q(J_{\boldsymbol{u}} - 1)\, d\boldsymbol{X}, \tag{9}$$

with $\boldsymbol{P}_{\boldsymbol{u}}$ denoting the first Piola–Kirchhoff stress given in Eq. (3), $\boldsymbol{F}_{\boldsymbol{u}}$ the deformation gradient tensor, and $J_{\boldsymbol{u}}$ its determinant (see Section 2). Similarly, for a given external energy term Π_t^k applied on the boundary Γ_0^k we can introduce a form $\mathcal{A}_t^k$ to denote the directional derivative of the external boundary term,

$$\mathcal{A}_t^k(\boldsymbol{u}, \boldsymbol{\lambda}_k; \boldsymbol{v}, \boldsymbol{\mu}_k) = \mathcal{D}_{(\boldsymbol{u},\boldsymbol{\lambda}_k)}\Pi_t^k(\boldsymbol{u}, \boldsymbol{\lambda}_k)[\boldsymbol{v}, \boldsymbol{\mu}_k]. \tag{10}$$

In this notation, the weak form problem can be written as: find $(\boldsymbol{u}, p, \boldsymbol{\lambda}) \in \boldsymbol{U} \times P \times \boldsymbol{\Lambda}$ such that,

$$\mathcal{A}_t(\boldsymbol{u}, p; \boldsymbol{v}, q) + \sum_{k \in \{b,l,e\}} \mathcal{A}_t^k(\boldsymbol{u}, \boldsymbol{\lambda}_k; \boldsymbol{v}, \boldsymbol{\mu}_k) = 0, \quad \forall\, (\boldsymbol{v}, q, \boldsymbol{\mu}) \in \boldsymbol{U} \times P \times \boldsymbol{\Lambda}. \tag{11}$$

In the subsequent sections, we will present different formulations for basal, endocardial and epicardial conditions as well as novel boundary energy potential terms proposed for patient-specific LV mechanics modeling.

3.1. Base plane boundary conditions

In studies of LV mechanics, the ventricular domain is often truncated. This approach avoids complications associated with modeling the basal tissue structure (that is dominated by fibroelastic connective tissue) and basal anatomy which is often poorly resolved in standard magnetic resonance or echocardiographic clinical imaging. Truncation of the myocardial geometry, however, introduces an artificial boundary, Γ_0^b, over which non-trivial boundary conditions are likely active.

A common approach in LV models is to impose some form of Dirichlet or mixed Dirichlet/zero-traction conditions (see Table 1). Assuming a known displacement $\boldsymbol{u}_d$ is available – either observable from imaging data or determinable by other means – many common conditions can be integrated using the boundary energy potential term (Eq. (12)) and its directional derivative (Eq. (13)), *i.e.*

$$\Pi_t^b(\boldsymbol{v}, \boldsymbol{\mu}_b) := \int_{\Gamma_0^b} \boldsymbol{\mu}_b \cdot (\boldsymbol{v} - \boldsymbol{u}_d(t))\ d\boldsymbol{X}, \tag{12}$$

$$\mathcal{A}_t^b(\boldsymbol{u}, \boldsymbol{\lambda}_b; \boldsymbol{v}, \boldsymbol{\mu}_b) := \int_{\Gamma_0^b} \boldsymbol{\lambda}_b \cdot \boldsymbol{v} + \boldsymbol{\mu}_b \cdot (\boldsymbol{u} - \boldsymbol{u}_d(t))\ d\boldsymbol{X}. \tag{13}$$

Typical conditions can be employed by careful selection of the space $\boldsymbol{\Lambda}_b$ (itself a subset of $\boldsymbol{\Lambda}$ from the previous section) containing the Lagrange multiplier $\boldsymbol{\lambda}_b$ and test variable $\boldsymbol{\mu}_b$ (also provided in Table 1 and discussed in Appendix A). For most conditions in Table 1, the presence of a Lagrange multiplier variable on the boundary introduces unnecessary added complexity to approaches where direct Dirichlet conditions are imposed. However, use of a Lagrange multiplier constraint to enforce these conditions was done in order to present the problem in the same manner and compare resultant boundary tractions.

Perhaps the most common condition using Eqs. (12) and (13) is the *fixed-base(0)* condition, which is straightforward to impose and popular if no other data is available. This condition is often applied to idealized analysis or for model testing. However, this condition is strict, often yielding unphysiological stresses and singularities in hydrostatic pressure. Moreover, in patient-specific simulations, this condition neglects base plane motion which may introduce both long-axis and short-axis motion throughout the LV model. *Fixed-base($\boldsymbol{u}_d$)* condition using data derived boundary motion provides a viable alternative, but success of this approach depends significantly on data quality.

Please cite this article in press as: L. Asner, et al., Patient-specific modeling for left ventricular mechanics using data-driven boundary energies, Comput. Methods Appl. Mech. Engrg. (2016), http://dx.doi.org/10.1016/j.cma.2016.08.002

Table 1
Summary of some common and proposed base plane conditions for LV mechanics models. Table provides a selection of references to models using these conditions, the typical manner in which the condition is integrated into the model, and how this can be implemented through boundary energy terms. ‡Fixed-In-Plane requires additional conditions to eliminate rotational modes. This is typically done by fixing opposing in-plane components on two nodes.

Base plane conditions			
Name	Eqn	Ref	Description
Fixed-base(0)	(12), (13)	[30,65]	Typically applied as $\boldsymbol{u} = \mathbf{0}$ Dirichlet zero condition. Assume $\boldsymbol{u}_d = \mathbf{0}$ and choose $\boldsymbol{\Lambda}_b = \gamma_b \boldsymbol{U}$.
Fixed-base($\boldsymbol{u}_d$)	(12), (13)	[26,66]	Typically applied as $\boldsymbol{u} = \boldsymbol{u}_d$ Dirichlet condition. Use data derived $\boldsymbol{u}_d$ and choose $\boldsymbol{\Lambda}_b = \gamma_b \boldsymbol{U}$.
Fixed-in-plane‡	(12), (13)	[8,67]	Typically applied as Dirichlet zero condition on through-plane component. Assume $\boldsymbol{u}_d \cdot \mathbf{n}_b = 0$ and choose $\boldsymbol{\Lambda}_b = \{\boldsymbol{\mu} \in \gamma_b \boldsymbol{U} \mid \boldsymbol{\mu} \cdot \mathbf{n}_1 = 0,\ \boldsymbol{\mu} \cdot \mathbf{n}_2 = 0\}$.
Fixed-endo-ring	(12), (13)	[68]	Typically applied as Dirichlet zero condition on $\Gamma_0^l \cap \Gamma_0^b$. Assume $\boldsymbol{u}_d = \mathbf{0}$ on $\Gamma_0^l \cap \Gamma_0^b$ and choose $\boldsymbol{\Lambda}_b = \{\boldsymbol{\mu} \in \gamma_b \boldsymbol{U} \mid \boldsymbol{\mu} = 0,\ \text{on } \Gamma_0^b \setminus \Gamma_0^l\}$.
Springs	–	[40,41]	The attachment of the base to the cardiac valves is modeled using linear springs, which allow for small valve motion.
Relaxed-base	(15)	[45,10]	Use data derived $\boldsymbol{u}_d$ and choose $\boldsymbol{\Lambda}_b = \gamma_b \boldsymbol{U}$.
Moments + relaxed-base	(18)	–	Use data derived $\boldsymbol{u}_d$ and choose $\boldsymbol{\Lambda}_b = [\mathbb{R}^3]^3 \times \gamma_b \boldsymbol{U}$.

Avoiding unphysiological stress and pressure peaks associated with Dirichlet conditions is an alternative technique employing springs to attach the base on the heart valves [40,41]. Contrary to the fixed base boundary condition, this technique enables a small degree of basal motion while avoiding strict enforcement of the constraint. Nevertheless, the motion introduced into the model is still substantially smaller compared to physiological motion observed *in vivo*.

In order to incorporate basal motion observed *in vivo*, Billet et al. proposed an image-based boundary condition. In particular, the basal motion applied on the model was estimated from the images by introducing an image force into the model dynamic equations [42,43].

An alternative is to apply penalty techniques [44], enabling some violation of conditions if excessive energy is required. This can be done using the *relaxed-base* condition [45,10],

$$\Pi_t^b(\boldsymbol{v}, \boldsymbol{\mu}_b) := \int_{\Gamma_0^b} \boldsymbol{\mu}_b \cdot \left(\boldsymbol{v} - \boldsymbol{u}_d - \frac{1}{2} \boldsymbol{K}_b(t) \boldsymbol{\mu}_b \right) \, d\boldsymbol{X}, \tag{14}$$

$$\mathcal{A}_t^b(\boldsymbol{u}, \boldsymbol{\lambda}_b; \boldsymbol{v}, \boldsymbol{\mu}_b) := \int_{\Gamma_0^b} \boldsymbol{\lambda}_b \cdot \boldsymbol{v} + \boldsymbol{\mu}_b \cdot [\boldsymbol{u} - \boldsymbol{u}_d(t) - \boldsymbol{K}_b(t) \boldsymbol{\lambda}_b] \, d\boldsymbol{X}, \tag{15}$$

where $\boldsymbol{K}_b$ is a penalty matrix, which can be chosen based on the accuracy of the data-derived motion $\boldsymbol{u}_d$. We note that this formulation shares similarities with the employment of springs and $\boldsymbol{K}_b$ could be thought analogously as a spring constant. However, in this case the reference position of the spring is adjusted dynamically by the data itself, making it conceptually different from the typical spring model. In [45,10], the penalty matrix $\boldsymbol{K}_b(t) = \varepsilon\big(\boldsymbol{I} - \mathbf{n}_b(t) \otimes \mathbf{n}_b(t)\big)$ was used to ensure that displacements in the direction of $\mathbf{n}_b$ are equivalent (weakly), while short-axis displacements are relaxed by the parameter ε.

While this relaxation prevents some potential artifacts due to imprecise data or image processing, noise in the base plane direction $\mathbf{n}_b$ is still imposed weakly on the model. In addition, the formulation does not ensure that some basic quantities are retained. Data averaged quantities, such as the mean position or the mean affine transformation, tend to minimize the impact of data noise and artifacts and should, therefore, be preserved. These quantities can be captured by considering the 0th and 1st moments of the data $\boldsymbol{u}_d$. To this end, we define $M_{m,n}[\boldsymbol{w}]$ as the m, nth moment of a function $\boldsymbol{w}$ on the base Γ_0^b. Specifically, we may define local coordinates aligned with the base plane axes, *e.g.* $\xi_i = (\mathbf{X} - \mathbf{X}_b) \cdot \boldsymbol{N}_i$ (see Fig. 2) where $\mathbf{X}_b$ is the mean position of the base and $\boldsymbol{N}_i$ the ith base vector ($i = 1, 2$). Using

Please cite this article in press as: L. Asner, et al., Patient-specific modeling for left ventricular mechanics using data-driven boundary energies, Comput. Methods Appl. Mech. Engrg. (2016), http://dx.doi.org/10.1016/j.cma.2016.08.002

this, the m, nth moment is defined as,

$$M_{m,n}[\boldsymbol{w}] := \int_{\Gamma_0^b} \omega^{m,n}(\mathbf{X})\, \boldsymbol{w}\ \ d\boldsymbol{X}, \quad \omega^{m,n} = \xi_1^m \xi_2^n. \tag{16}$$

From Eq. (16), we see that the zero moment $M_{0,0}$ provides mean quantities. For example, $M_{0,0}[\mathbf{X}] = \mathbf{X}_b$ provides the mean position of the base and $M_{0,0}[\boldsymbol{u}_d] = \boldsymbol{u}_0$ the mean displacement of the base plane. Hence, requiring $M_{0,0}[\boldsymbol{u} - \boldsymbol{u}_d] = \mathbf{0}$ constrains the mean quantity of the model to match that of the data. Similarly, constraining first order moments $M_{1,0}$ and $M_{0,1}$ ensures conditions of the optimal affine transformation are preserved in the model. To see this, we can define the best affine transformation $\boldsymbol{A}$ as

$$\boldsymbol{A} = \min_{\boldsymbol{M}\in\mathbb{R}^{3\times 2}} \frac{1}{2} \int_{\Gamma_0^b} |\boldsymbol{u}_{\boldsymbol{M}} - \boldsymbol{u}_d|^2 \ \ d\boldsymbol{X}$$

where $\boldsymbol{u}_{\boldsymbol{M}} = \boldsymbol{M}(\xi_1, \xi_2)^T + \boldsymbol{u}_0$ is an affine function on the plane. Taking the derivative with respect to components of the generic matrix $\boldsymbol{M}$, it can be shown that the optimal affine transformation must satisfy the constraints

$$\int_{\Gamma_0^b} \xi_i (\boldsymbol{u}_{\boldsymbol{A}} - \boldsymbol{u}_d)\ \ d\boldsymbol{X}, \quad i = 1, 2$$

or equivalently, that $M_m[\boldsymbol{u}_{\boldsymbol{A}} - \boldsymbol{u}_d] = 0$ for $m = (1, 0)$ and $(0, 1)$. As these integrative quantities are less subject to data errors, we propose that the zero and first moments of the base plane – $M_{0,0}$, $M_{1,0}$, $M_{0,1}$ – should be consistent between the data and model. To achieve this, we propose a *moments + relaxed-base* condition, *i.e.*

$$\Pi_t^b(\boldsymbol{v}, \{\boldsymbol{\mu}_b^k\}) := \sum_m \boldsymbol{\mu}_b^m \cdot M_m[\boldsymbol{v} - \boldsymbol{u}_d(t)] + \int_{\Gamma_0^b} \boldsymbol{\mu}_b \cdot \left(\boldsymbol{v} - \boldsymbol{u}_d(t) - \frac{1}{2}\boldsymbol{\Sigma}\boldsymbol{\mu}_b\right)\ \ d\boldsymbol{X} \tag{17}$$

$$\begin{aligned}\mathcal{A}_t^b(\boldsymbol{u}, \{\boldsymbol{\lambda}_b^k\}; \boldsymbol{v}, \{\boldsymbol{\mu}^k\}) := &\sum_m \boldsymbol{\lambda}_b^m \cdot M_m[\boldsymbol{v}] + \sum_m \boldsymbol{\mu}_b^m \cdot M_m[\boldsymbol{u} - \boldsymbol{u}_d(t)] \\ &+ \int_{\Gamma_0^b} \boldsymbol{\lambda}_b \cdot \boldsymbol{v} + \boldsymbol{\mu}_b \cdot [\boldsymbol{u} - \boldsymbol{u}_d(t) - \boldsymbol{\Sigma}\boldsymbol{\lambda}_b]\ \ d\boldsymbol{X}\end{aligned}$$

$$\text{for } m = \{0, 0\}, \{1, 0\}, \{0, 1\} \tag{18}$$

where $\{\boldsymbol{\lambda}_b^k\} = \{\boldsymbol{\lambda}_b^{0,0}, \boldsymbol{\lambda}_b^{1,0}, \boldsymbol{\lambda}_b^{0,1}, \boldsymbol{\lambda}_b\} \in [\mathbb{R}^3]^3 \times \gamma_b \boldsymbol{U}$ is a partitioning of the boundary traction into its 0th order moments ($\boldsymbol{\lambda}_b^{0,0}$), 1st order moments ($\boldsymbol{\lambda}_b^{1,0}, \boldsymbol{\lambda}_b^{0,1}$) and higher order effects ($\boldsymbol{\lambda}_b$). Here, $\boldsymbol{\lambda}_b^{0,0}, \boldsymbol{\lambda}_b^{1,0}, \boldsymbol{\lambda}_b^{0,1}$ denote Lagrange multipliers constraining equality of the indicated moments between data and model and $\boldsymbol{\lambda}_b$ denotes a penalty variable which can be used to constrain base plane motion towards the data. Similarly, $\{\boldsymbol{\mu}^k\} = \{\boldsymbol{\mu}_b^0, \boldsymbol{\mu}_b^{1,0}, \boldsymbol{\mu}_b^{0,1}, \boldsymbol{\mu}_b\} \in [\mathbb{R}^3]^3 \times \gamma_b \boldsymbol{U}$. Relaxation is controlled by the matrix $\boldsymbol{\Sigma}$, which we tune asymmetrically in the long-axis and base plane due to inherent differences in the expected forces as well as potential asymmetry in data accuracy, *i.e.*

$$\boldsymbol{\Sigma} = \varepsilon_{la} \boldsymbol{N}_b \otimes \boldsymbol{N}_b + \varepsilon_{sa}(\boldsymbol{I} - \boldsymbol{N}_b \otimes \boldsymbol{N}_b), \quad \varepsilon_{la}, \varepsilon_{sa} > 0.$$

In this formulation, only integrated quantities are imposed strictly – *i.e.* mean point and the best fit affine map to the data – while more stringent conditions on base plane motion stemming from data may be relaxed using ε_{la} and ε_{sa} to minimize the influence of potential artifacts to the mathematical model. By design, the formulation ensures that $\boldsymbol{\lambda}_b$ satisfies,

$$M_{0,0}[\boldsymbol{\lambda}_b] = M_{1,0}[\boldsymbol{\lambda}_b] = M_{0,1}[\boldsymbol{\lambda}_b] = \mathbf{0},$$

and that uniqueness is retained in the variables $\{\boldsymbol{\lambda}_b^k\}$ (under suitable assumptions on the original model problem). Briefly, this can be seen by examining $\mathcal{A}_t^b$. Choosing all other test function to be zero and varying $\{\boldsymbol{\mu}_b^0, \boldsymbol{\mu}_b^{1,0}, \boldsymbol{\mu}_b^{0,1}\}$ individually, we see that these moments match between data and model. Hence, choosing all other test function to be zero and selecting $\boldsymbol{\mu}_b$ to be a vector with each component equal to 1, ξ_1 or ξ_2 we arrive at the above constraints on $\boldsymbol{\lambda}_b$.

Please cite this article in press as: L. Asner, et al., Patient-specific modeling for left ventricular mechanics using data-driven boundary energies, Comput. Methods Appl. Mech. Engrg. (2016), http://dx.doi.org/10.1016/j.cma.2016.08.002

Table 2
Summary of some common and proposed endocardial boundary conditions for LV mechanics models. Table provides a selection of references to models using these conditions, the typical manner in which the condition is integrated into the model, and how this can be implemented through boundary energy terms.

Endocardial conditions			
Name	Eqn	Ref	Description
Endo-pressure	(19)	[12,52,31,40]	Typically applied using measured/literature/model derived $-P_{lv}$ in the normal direction on Γ^l. Iso-volumic phases controlled using iterative approach
Endo-volume	(21), (22)	[45,69]	Applied using $\Lambda_e = \mathbb{R}$ and using data-derived V_{lv}. Methods vary in how $V(\boldsymbol{u})$ is computed: SVI: V calculated using Eq. (24) VI: V calculated using Eq. (28)
Endo-volume-rate	(26)	[56,66]	Applied using $\Lambda_e = \mathbb{R}$ and using data-derived $\partial_t V_{lv}$. VRI: V calculated using Eq. (26)

3.2. Endocardial boundary conditions

The endocardial surface of the LV is comprised of myocardial muscle, trabeculae and papillary muscles that are interacting with intraventricular flows [46]. Typically, the complexity of cardiac anatomy is simplified to consider only the myocardial muscle, neglecting the presence of trabeculae and papillary muscles which serve support roles in contraction. The interaction of muscle and blood flow can yield complex hemodynamics and momentum transfer. While in some disease cases, such as congenital heart disease [47] or valve stenosis [48,49], hemodynamic effects can play an important role, in many circumstances the mechanics of the heart are principally dominated by hemodynamic pressure (with minimal influence of shear stress). It has been shown both experimentally [50] and numerically [51] that momentum effects yield spatial variation in the left ventricular fluid pressure. However, apart from early diastolic and systolic phases, these variations in pressure are usually $<5\%$ of the mean pressure, making spatial variability in pressure less significant in predicting muscle behavior.

As a result, most LV mechanics models assume a constant intraventricular lumen pressure, P_{lv}. This pressure can be either derived from data, tuned through use of Windkessel models [52] or inferred at some or all states through the heart cycle [21]. Integration of endocardial constraints can be employed through multiple mechanisms (see Table 2), perhaps the most common of which is through direct imposition of pressure data by a surface traction $\boldsymbol{t}_{lv}$, *i.e.*

$$\Pi_t^l(\boldsymbol{v}) := \int_{\Gamma_0^l} \boldsymbol{t}_{lv}(t) \cdot \boldsymbol{v} \; dA \tag{19}$$

$$\mathcal{A}_t^l(\boldsymbol{u};\boldsymbol{v}) := -P_{lv}(t) \int_{\Gamma_0^l} \boldsymbol{v} \cdot J_{\boldsymbol{u}} \boldsymbol{F}_{\boldsymbol{u}}^{-T} \boldsymbol{N} \; dA, \tag{20}$$

where $\boldsymbol{t}_{lv}$ is considered *given data* in Eq. (19) and is subsequently related to the pressure (using Nanson's formula [39]) by $\boldsymbol{t}_{lv} = -P_{lv} J \boldsymbol{F}^{-T} \boldsymbol{N}$. This boundary constraint is commonly used in cardiac mechanical models of both animals [31] and humans [26]. However, this approach requires *a priori* knowledge of the intraventricular pressure throughout the cardiac cycle. While some non-invasive techniques are under development [21,53], measurement of intraventricular pressure is currently dependent on cardiac catheterization, limiting the application of this model to patients who will undergo this invasive procedure. Additional complexity occurs during isovolumetric phases of the cardiac cycle, where the changing activation of the heart muscle leads to a variable increase or decrease in pressure, while the LV cavity volume, V_{lv}, remains constant. These phases can be addressed by iteratively solving for the pressure yielding negligible volume change [31].

An alternative approach is to instead impose the volume, V_{lv}, of the LV cavity directly. In this approach, V_{lv} may be defined based on non-invasive imaging data taken throughout the cardiac cycle. This volume driven approach can be achieved by changing Π_t^l to denote the boundary energy required to achieve the volume V_{lv}. It also provides a more straightforward approach for full cycle simulations by eliminating the need to apply iterative approaches to manage

Please cite this article in press as: L. Asner, et al., Patient-specific modeling for left ventricular mechanics using data-driven boundary energies, Comput. Methods Appl. Mech. Engrg. (2016), http://dx.doi.org/10.1016/j.cma.2016.08.002

isovolumetric phases of the heart cycle. Introducing a Lagrange multiplier, $\lambda_l(t) \in \Lambda_l = \mathbb{R}$, the energy constraint can be written as,

$$\Pi_t^l(\boldsymbol{v}, \mu_l) := \mu_l[V(\boldsymbol{v}, t) - V_{lv}(t)], \tag{21}$$

$$\mathcal{A}_t^l(\boldsymbol{u}, \lambda_l; \boldsymbol{v}, \mu_l) := -\lambda_l \int_{\Gamma_0^l} \boldsymbol{v} \cdot J_{\boldsymbol{u}} \boldsymbol{F}_{\boldsymbol{u}}^{-T} \boldsymbol{N} \; d\boldsymbol{X} + \mu_l[V(\boldsymbol{u}, t) - V_{lv}(t)], \tag{22}$$

with the volume $V(\boldsymbol{u}, t)$ computed using the boundary integral over the truncated LV lumen,

$$V(\boldsymbol{u}, t) = \frac{1}{3}\left(\int_{\Gamma_0^l} (\boldsymbol{u} + \mathbf{X}) \cdot \tilde{\mathbf{n}}_l \; d\boldsymbol{X} + \int_{\Gamma^{lv,t}} (\boldsymbol{u}_d(t) + \mathbf{X}) \cdot \mathbf{n}_b \; d\boldsymbol{x}\right). \tag{23}$$

In Eq. (23) the second term gives the effective flux of volume due to motion of the top of the lumen (denoted $\Gamma^{lv,t}$) and can be derived from the data. In Eq. (23) we assume that $\tilde{\mathbf{n}}_l$ (the area weighted outward normal of the LV lumen domain Ω_{lv}) is given, replacing $\tilde{\mathbf{n}}_l = -J_{\boldsymbol{u}} \boldsymbol{F}_{\boldsymbol{u}}^{-T} \boldsymbol{N}$ in Eq. (22) using Nanson's formula. Note, a change of variables is performed on λ_l to eliminate the additional factor $1/3$.

Methods of volume prescription in Eq. (22) vary in the literature. One simplification is to assume negligible base plane motion in Eq. (23), computing the model-derived volume V in Eq. (22) as,

$$V_{SVI}(\boldsymbol{u}, t) = -\frac{1}{3}\int_{\Gamma_0^l} (\boldsymbol{u} + \mathbf{X}) \cdot J_{\boldsymbol{u}} \boldsymbol{F}_{\boldsymbol{u}}^{-T} \boldsymbol{N} \; d\boldsymbol{X}. \tag{24}$$

Here we note that this formulation requires re-orienting the heart so $\boldsymbol{x} \cdot \mathbf{n}_b = 0$ on the base (e.g. translation/rotation so the base plane integral goes to zero). Another approach which avoids re-orienting the model can be derived using the Spatial Conservation Law [54]. Noting that,

$$\partial_t V(\boldsymbol{u}, t) = \partial_t \int_{\Omega_{lv}} d\boldsymbol{x} = \int_{\Omega_{lv}} \nabla \cdot \partial_t \boldsymbol{u} \; d\boldsymbol{x} = \int_{\Gamma_0^l} \partial_t \boldsymbol{u} \cdot \tilde{\mathbf{n}} \; d\boldsymbol{X} + \int_{\Gamma^{lv,t}} \boldsymbol{v}_b \cdot \mathbf{n}_b \; d\boldsymbol{x}, \tag{25}$$

under assumptions of negligible base plane velocity $\boldsymbol{v}_b$, we can compare the rate of volume change with the known increase/decrease in volumes by replacing $[V(\boldsymbol{u}) - V_{lv}]$ with $[V_{VRI}(\boldsymbol{u}(t)) - \partial_t V_{lv}(t)]$ in Eq. (22) and computing,

$$V_{VRI}(\boldsymbol{u}, t) = -\int_{\Gamma_0^l} \partial_t \boldsymbol{u} \cdot J_{\boldsymbol{u}} \boldsymbol{F}_{\boldsymbol{u}}^{-T} \boldsymbol{N} \; d\boldsymbol{X}. \tag{26}$$

Both V_{SVI} and V_{VRI} are valid when base plane motion is minimal but may introduce a potential bias when motion is observed. However, this assumption can be easily compensated for by noting that the volume formula in Eq. (23) is not unique, but instead exploits the divergence theorem. In general, we may compute the cavity volume based purely on the motion of the endocardial cavity boundary. In this case, we seek a vector function $\boldsymbol{g}$ that satisfies,

$$V = \int_{\Omega_{lv}} \nabla \cdot \boldsymbol{g}(\boldsymbol{x}) \; d\boldsymbol{x} = \int_{\Gamma_0^l} \boldsymbol{g}(\boldsymbol{x}) \cdot \tilde{\mathbf{n}}_l \; d\boldsymbol{X}. \tag{27}$$

Assuming that the base plane maintains planarity throughout the cardiac cycle, we may select the simple form $\boldsymbol{g}(\boldsymbol{x}) = \boldsymbol{I}_b(t)\boldsymbol{x}$, with $\boldsymbol{I}_b(t) = (1/2)(\boldsymbol{I} - \mathbf{n}_b(t) \otimes \mathbf{n}_b(t))$ Here, we observe

$$\int_{\Omega_{lv}} \nabla \cdot \boldsymbol{g}(\boldsymbol{x}) \; d\boldsymbol{x} = \frac{1}{2}(\boldsymbol{I} - \mathbf{n}_b \otimes \mathbf{n}_b) : \int_{\Omega_{lv}} \nabla \boldsymbol{x} \; d\boldsymbol{x} = \frac{1}{2} V(\boldsymbol{I} - \mathbf{n}_b \otimes \mathbf{n}_b) : \boldsymbol{I} = V.$$

Moreover, due to the assumed planarity and using Divergence theorem,

$$\int_{\Omega_{lv}} \nabla \cdot \boldsymbol{g}(\boldsymbol{x}) \; d\boldsymbol{x} = \int_{\Gamma_0^l} \boldsymbol{g}(\mathbf{X} + \boldsymbol{u}) \cdot \tilde{\mathbf{n}}_l \; d\boldsymbol{X} + \int_{\Gamma^{lv,t}} \boldsymbol{g}(\boldsymbol{x}) \cdot \mathbf{n}_b \; d\boldsymbol{x} = \int_{\Gamma_0^l} \boldsymbol{g}(\mathbf{X} + \boldsymbol{u}) \cdot \tilde{\mathbf{n}}_l \; d\boldsymbol{X}$$

Please cite this article in press as: L. Asner, et al., Patient-specific modeling for left ventricular mechanics using data-driven boundary energies, Comput. Methods Appl. Mech. Engrg. (2016), http://dx.doi.org/10.1016/j.cma.2016.08.002

where we note $\boldsymbol{g}(\boldsymbol{x}) \cdot \mathbf{n}_b = 0$ for any $\boldsymbol{x}$. Hence, we propose to compute the model derived volume in Eq. (22) using

$$V_{VI}(\boldsymbol{u}, t) := -\int_{\Gamma_0^l} \boldsymbol{I}_b(t)(\boldsymbol{u} + \mathbf{X}) \cdot J_{\boldsymbol{u}} \boldsymbol{F}_{\boldsymbol{u}}^{-T} \boldsymbol{N}\, d\boldsymbol{X}. \tag{28}$$

3.3. Epicardial boundary conditions

The epicardial constraint on the left ventricular myocardium is arguably the least well characterized. Although some studies have introduced a fixed pericardial surface to constrain the epicardial motion [41,40], in most cases, the uncertainty concerning the forces applied on the epicardial wall has led to the external energy on the epicardium being set to zero, *i.e.* $\Pi_t^e(\boldsymbol{v}) = 0$. Though the heart is surrounded by the fibrous pericardial sac and is adjacent to the diaphram, ribcage and lungs, this assumption is based on the premise that the boundary energies coming from the epicardium are negligible compared to the other boundary energies present.

However, similar to the base of the LV, truncation is also introduced along the LV/RV junction (RV denotes the right ventricle). This is likely to introduce non-negligible forces on the LV heart wall, owing to both filling and contraction in the right ventricle. To account for this missing force, we propose the following energy model on the epicardium,

$$\Pi_t^e(\boldsymbol{v}, \boldsymbol{\mu}_e) := \int_{\Gamma_0^e} H \boldsymbol{\mu}_e \cdot \left(\boldsymbol{v} - \boldsymbol{u}_d(t) - \frac{\varepsilon_e}{2} \boldsymbol{\mu}_e \right) d\boldsymbol{X} \tag{29}$$

$$\mathcal{A}_t^e(\boldsymbol{u}, \boldsymbol{\lambda}_e; \boldsymbol{v}, \boldsymbol{\mu}_e) := \int_{\Gamma_0^e} \boldsymbol{\lambda}_e \cdot \boldsymbol{w} + \boldsymbol{\mu}_e \cdot [H(\boldsymbol{u} - \boldsymbol{u}_d(t)) - \varepsilon_e \boldsymbol{\lambda}_e]\, d\boldsymbol{X} \tag{30}$$

where $\boldsymbol{\lambda}_e$ is an added penalty variable defined on the epicardial surface (and $\boldsymbol{\mu}_e$ the corresponding test function), $\varepsilon_e > 0$ is a relaxation parameter and $H : \Omega_0 \to [0, 1]$ is a scalar function labeling the RV/LV junction (1) and epicardial/septal surfaces (0) as derived from images (see Fig. 3). In this case, the epicardial boundary energy is introduced to account for the potential traction stemming from right ventricular filling and contraction through the penalty variable $\boldsymbol{\lambda}_e \in \gamma_e \boldsymbol{U}$ defined on the entire epicardium. While forces are only required at the LV/RV junction, extension to the entirety of Γ_0^e is performed in order to ease the need for developing complex boundary domains. For this reason, a change of variables $\boldsymbol{\lambda}_e = H\boldsymbol{\lambda}_e$ is applied from Π_t^e to $\mathcal{A}_t^e$ to ensure solvability of the penalty variable $\boldsymbol{\lambda}_e$ over the entire epicardial region.

4. Discretization and solution

To simulate the LV cardiac model, the time interval $(0, T]$ was discretized into time points $\{t_1, \ldots, t_N\}$ starting from end diastole and transitioning through the heart cycle. Patient-specific input data – e.g. $\boldsymbol{u}_d$, V_{lv}, $\mathbf{n}_b$ – is interpolated from imaging sources to the $n = 1, \ldots, N$ time steps. The reference domain Ω_0 is then split into tetrahedral or curvilinear hexahedral elements and displacement–pressure state variables are interpolated using quadratic–linear Taylor–Hood elements (details on interpolations can be found in Table 3 and meshes in Table 4). Spaces $\boldsymbol{U}^h$ and P^h (discrete displacement and pressure spaces) are constructed in the standard way, and required boundary tractions are constructed from the trace restricted to the appropriate subset boundary (see Appendix A).

At each time point t_n, we then look to find the displacement, pressure and boundary tractions/pressures $(\boldsymbol{u}_h, p_h, \{\boldsymbol{\lambda}_{h,k}\}) \in \boldsymbol{U}^h \times P^h \times \boldsymbol{\Lambda}^h$ such that,

$$\mathcal{A}_{t_n}(\boldsymbol{u}_h, p_h; \boldsymbol{v}_h, q_h) + \sum_{k \in \{b,l,e\}} \mathcal{A}_{t_n}^k(\boldsymbol{u}_h, \boldsymbol{\lambda}_{h,k}; \boldsymbol{v}_h, \boldsymbol{\mu}_{h,k}) = 0, \quad \forall (\boldsymbol{v}_h, q_h, \{\boldsymbol{\mu}_{h,k}\}) \in \boldsymbol{U}^h \times P^h \times \boldsymbol{\Lambda}^h. \tag{31}$$

Note that, for ease of notation, we omit the reference to the current timestep (*e.g.* $\boldsymbol{u}_h = \boldsymbol{u}_h(t_n)$ in Eq. (31)). The final form depends on the selected boundary energies, hence we leave the actual defined multipliers in Eq. (31) general. However, for the proposed patient-specific LV model, $\{\mathcal{A}_b, \mathcal{A}_l, \mathcal{A}_e\}$ are defined using Eqs. (18), (22), (28) and (30). Here, $\{\boldsymbol{\lambda}_{h,k}\} = \{\boldsymbol{\lambda}_b^{0,0}, \boldsymbol{\lambda}_b^{1,0}, \boldsymbol{\lambda}_b^{0,1}, \boldsymbol{\lambda}_b, \lambda_l, \boldsymbol{\lambda}_e\}$ denotes the group of boundary multipliers and penalty variables introduced on boundaries of the model and the resultant space $\boldsymbol{\Lambda}^h$ is defined as

$$\boldsymbol{\Lambda}^h = [\mathbb{R}^3]^3 \times \gamma_b \boldsymbol{U}^h \times \mathbb{R} \times \gamma_e \boldsymbol{U}^h$$

Please cite this article in press as: L. Asner, et al., Patient-specific modeling for left ventricular mechanics using data-driven boundary energies, Comput. Methods Appl. Mech. Engrg. (2016), http://dx.doi.org/10.1016/j.cma.2016.08.002

Table 3
Summary of finite element interpolations used for the LV mechanics model. Here, W denotes the basis matrix and U the coefficient vector for each variable. Note that the total rank of the system, $\mathtt{N}_T = 3\mathtt{N}_{\boldsymbol{u}} + \mathtt{N}_p + 3\mathtt{N}_b + 3\mathtt{N}_e + 9$. $\mathtt{N}_{\boldsymbol{u}}$ = no. displacement nodes, $\mathtt{N}_p$ = no. pressure nodes, $\mathtt{N}_b$ = no. base plane displacement nodes, $\mathtt{N}_e$ = no. epi displacement nodes.

Finite element implementation

Variable	Interpolation	Notation
$\boldsymbol{u}_h = W^{\boldsymbol{u}} U^{\boldsymbol{u}}$	$\mathbb{Q}^2(\mathtt{HEX})$ or $\mathbb{P}^2(\mathtt{TET})$	$U^{\boldsymbol{u}} \in \mathbb{R}^{3\mathtt{N}_{\boldsymbol{u}}}$ $W^{\boldsymbol{u}} : \Omega_0 \to \mathbb{R}^{3\times 3\mathtt{N}_{\boldsymbol{u}}}$ $W^{\boldsymbol{u}} = [\varphi_1^{\boldsymbol{u}}\mathbf{e}_1, \varphi_1^{\boldsymbol{u}}\mathbf{e}_2, \ldots, \varphi_{\mathtt{N}_{\boldsymbol{u}}}^{\boldsymbol{u}}\mathbf{e}_3]$
$p_h = W^p U^p$	$\mathbb{Q}^1(\mathtt{HEX})$ or $\mathbb{P}^1(\mathtt{TET})$	$U^p \in \mathbb{R}^{\mathtt{N}_p}$ $W^p : \Omega_0 \to \mathbb{R}^{1\times \mathtt{N}_p}$ $W^p = [\varphi_1^p, \ldots, \varphi_{\mathtt{N}_p}^p]$
$\boldsymbol{\lambda}_{h,b}^k = W^b U^{b,k}$	$[\mathbb{R}^3]^3, \mathbb{Q}^2(\mathtt{SQ})$ or $[\mathbb{R}^3]^3, \mathbb{P}^2(\mathtt{TRI})$	$U^{b,k} \in \mathbb{R}^3, U^b \in \mathbb{R}^{3\mathtt{N}_b}$ $W^{b,k} : \Omega_0 \to \mathbb{R}^3, W^b : \Omega_0 \to \mathbb{R}^{3\times 3\mathtt{N}_b}$, $W^{b,k} = [\boldsymbol{I}\omega^k]$, $W^b = [\varphi_1^b\mathbf{e}_1, \varphi_1^b\mathbf{e}_2, \ldots, \varphi_{\mathtt{N}_b}^b\mathbf{e}_3]$. (for $k = \{0,0\}, \{1,0\}, \{0,1\}$)
$\lambda_{h,l} = W^l U^l$	$\mathbb{R}$	$U^l \in \mathbb{R}$ $W^l : \Omega_0 \to 1$
$\boldsymbol{\lambda}_{h,e} = W^e U^e$	$\mathbb{Q}^2(\mathtt{SQ})$ or $\mathbb{P}^2(\mathtt{TRI})$	$U^e \in \mathbb{R}^{3\mathtt{N}_e}$ $W^e : \Omega_0 \to \mathbb{R}^{3\times 3\mathtt{N}_e}$ $W^e = [\varphi_1^e\mathbf{e}_1, \varphi_1^e\mathbf{e}_2, \ldots, \varphi_{\mathtt{N}_e}^e\mathbf{e}_3]$

at each time step. In the usual way, the FEM discrete weak form problem in Eq. (31) can be equivalently written as the root to the vector function $\boldsymbol{R} : \mathbb{R}^{\mathtt{N}_T} \to \mathbb{R}^{\mathtt{N}_T}$. Noting that, from Table 3, the state variables, boundary tractions and pressures can be written as a weighted sum WU, with

$$WU = \begin{bmatrix} \boldsymbol{u} \\ p \\ \boldsymbol{\lambda}_b^{0,0} \\ \boldsymbol{\lambda}_b^{1,0} \\ \boldsymbol{\lambda}_b^{0,1} \\ \boldsymbol{\lambda}_b \\ \lambda_l \\ \boldsymbol{\lambda}_e \end{bmatrix}, \quad W = \left[W^{\boldsymbol{u}}, W^p, W^{b^{0,0}}, W^{b^{1,0}}, W^{b^{0,1}}, W^b, W^l, W^e\right], \quad U = \begin{bmatrix} U^{\boldsymbol{u}} \\ U^p \\ U^{b^{0,0}} \\ U^{b^{1,0}} \\ U^{b^{0,1}} \\ U^b \\ U^l \\ U^e \end{bmatrix}.$$

Eq. (31) can be written concisely as a function of the unknown weights U and V of the trial and test function coefficients, *i.e.*

$$A_{t_n}(U, V) := \mathcal{A}_{t_n}(W^{\boldsymbol{u}}U^{\boldsymbol{u}}, W^pU^p; W^{\boldsymbol{u}}V^{\boldsymbol{u}}, W^pV^p) + \sum_{k\in\{b,l,e\}} \mathcal{A}_{t_n}^k(W^{\boldsymbol{u}}U^{\boldsymbol{u}}, W^kU^k; W^{\boldsymbol{u}}V^{\boldsymbol{u}}, W^kV^k).$$

Here W^k denotes a vector of all basis functions used for the k-variable (see Table 3) and similarly U^k denotes the corresponding weights. Hence, the solution U is a root of the residual vector function $\boldsymbol{R}$ given as,

$$\boldsymbol{R}(U) = \nabla_V A_{t_n}(U, V) = \mathbf{0}. \tag{32}$$

The general solution procedure to solve Eq. (32) is outlined in Algorithm 1. Briefly, we follow a Shamanskii–Newton Raphson procedure introduced previously in [55] and used in [56]. Here, the Jacobian matrix, $\mathcal{K}$, and its inverse are initially computed and only recomputed when residual convergence slows. This is controlled by the parameter $\gamma \in (0, 1)$, which dictates the minimum relative decrease required in the residual vector function (here $\gamma = 0.75$ was used). The Jacobian matrix itself is computed as $\mathcal{K} = \nabla_U \boldsymbol{R}$ which, owing to the structure of boundary energy terms,

Please cite this article in press as: L. Asner, et al., Patient-specific modeling for left ventricular mechanics using data-driven boundary energies, Comput. Methods Appl. Mech. Engrg. (2016), http://dx.doi.org/10.1016/j.cma.2016.08.002

Table 4
Table of sizes for different computational meshes used for idealized and patient-specific meshes. $\mathtt{N}_E$ = no. of elements, $\mathtt{N}_{\boldsymbol{u}}$ = no. of nodes for displacement, $\mathtt{N}_p$ = no. of nodes for hydrostatic pressure, $\mathtt{N}_b$ = no. of nodes for basal penalty variable, $\mathtt{N}_e$ = no. of nodes for the epicardial multiplier. $E[h]$ and $\sigma(h)$ denote mean and standard deviation of the mesh size h.

Idealized mesh

	$\mathtt{N}_E$	$E[h] \pm \sigma(h)$	$(\mathtt{N}_{\boldsymbol{u}}; \mathtt{N}_p)$	$\mathtt{N}_b$	$\mathtt{N}_e$
	448	8.30 ± 2.31	(4,185; 605)	289	465

Volunteer/Patient meshes

	$\mathtt{N}_E$	$E[h] \pm \sigma(h)$	$(\mathtt{N}_{\boldsymbol{u}}; \mathtt{N}_p)$	$\mathtt{N}_b$	$\mathtt{N}_e$
V1	17,153	3.33 ± 0.53	(27,589; 4,048)	574	4,852
V2	6,787	3.88 ± 1.09	(12,657; 2,050)	451	3,735
V3	7,795	4.34 ± 0.34	(13,499; 2,088)	543	3,372
P1	10,740	3.90 ± 0.56	(18,104; 2,747)	487	3,913
P2	17,047	3.47 ± 0.53	(28,012; 4,173)	629	5,487
P3	10,731	3.45 ± 0.67	(19,025; 2,986)	632	4,688

can be written as,

$$\mathcal{K} := \begin{bmatrix} \mathcal{A} & \mathcal{B} \\ \mathcal{C} & \mathcal{D} \end{bmatrix}, \qquad \mathcal{A} := \mathcal{K}_{V^{\boldsymbol{u}},U^{\boldsymbol{u}}},$$

$$\mathcal{B} := \left[\mathcal{K}_{V^{\boldsymbol{u}},U^p},\ \mathcal{K}^b_{V^{\boldsymbol{u}},U^{b^{0,0}}},\ \mathcal{K}^b_{V^{\boldsymbol{u}},U^{b^{1,0}}},\ \mathcal{K}^b_{V^{\boldsymbol{u}},U^{b^{0,1}}},\ \mathcal{K}^b_{V^{\boldsymbol{u}},U^b},\ \mathcal{K}^l_{V^{\boldsymbol{u}},U^l},\ \mathcal{K}^e_{V^{\boldsymbol{u}},U^e} \right]$$

$$\mathcal{C} := \begin{bmatrix} \mathcal{K}_{V^p,U^{\boldsymbol{u}}} \\ \mathcal{K}^b_{V^{b^{0,0}},U^{\boldsymbol{u}}} \\ \mathcal{K}^b_{V^{b^{1,0}},U^{\boldsymbol{u}}} \\ \mathcal{K}^b_{V^{b^{0,1}},U^{\boldsymbol{u}}} \\ \mathcal{K}^b_{V^b,U^{\boldsymbol{u}}} \\ \mathcal{K}^l_{V^l,U^{\boldsymbol{u}}} \\ \mathcal{K}^e_{V^e,U^{\boldsymbol{u}}} \end{bmatrix}, \quad \mathcal{D} := \begin{bmatrix} \mathbf{0} & \cdots & \cdots & \cdots & \cdots & \cdots & \mathbf{0} \\ \vdots & \ddots & & & & & \vdots \\ \vdots & & \ddots & & & & \vdots \\ \vdots & & & \mathbf{0} & & & \vdots \\ \vdots & & & & \mathcal{K}^b_{V^b,U^b} & & \vdots \\ \vdots & & & & & 0 & 0 \\ \mathbf{0} & \cdots & \cdots & \cdots & \cdots & 0 & \mathcal{K}^e_{V^e,U^e} \end{bmatrix}$$

with $\mathcal{K}^k_{V^\beta,U^\alpha}$ denoting the sub block matrix corresponding to the derivative with respect to the indicated variables, *i.e.*

$$\mathcal{K}^k_{V^\beta,U^\alpha} = \nabla_{U^\alpha} \nabla_{V^\beta} A^k_{t_n}(U, V), \quad \left[\mathcal{K}^k_{V^\beta,U^\alpha}\right]_{ij} = \frac{\partial^2 A^k_t(U, V)}{\partial U^\alpha_i \partial V^\beta_j} \tag{33}$$

and $A^k_{t_n}$ denoting the individual operators $\mathcal{A}^k_{t_n}$. All model components were implemented and solved in $\mathcal{C}$ Heart—a multiphysics solver developed at King's College London [57] and used in a number of cardiac modeling projects [58,59,10,60,61].

5. Model problems

5.1. Idealized LV model

The boundary conditions introduced in Sections 3.1–3.3 were initially tested using *in silico* passive inflation of an idealized LV. The LV was modeled as a thick-walled truncated ellipsoid of physiological cardiac dimensions. A quadratic hexahedral mesh was used to solve the discretized problem with dimensions as described in Table 4. Consistent physiological values of end-diastolic pressure and volume were used as end-point for inflation depending

Algorithm 1 `Cardiac Mechanics Solve.`

Given: reference state U^0.
`Compute` $\mathcal{K} = \nabla_U \boldsymbol{R}(U^0)$, $\mathcal{K}^{-1}$.

for $(n = 1 : N)$ **do**
  `Set` $k = 0$, $U^{n,k} = U^{n-1}$.
  `Compute` $\boldsymbol{R}(U^{n,k})$, $r = c\|\boldsymbol{R}(U^{n,k})\|$.

  while $(r > TOL)$ **do**
    `Compute` $\Delta U = -\mathcal{K}^{-1}\boldsymbol{R}(U^{n,k})$.
    `Find` $\tilde{r} = \min\left\{\|\boldsymbol{R}(U^{n,k+1})\|,\ U^{n,k+1} = U^{n,k} + \alpha\ \Delta U,\ \alpha \in [0, 1]\right\}$.
    if $(\tilde{r} > \gamma\ r$ or $k > ITER)$ **then**
      `Compute` $\mathcal{K} = \nabla_U \boldsymbol{R}(U^{n,k+1})$, $\mathcal{K}^{-1}$.
    `Set` $r = \tilde{r}$, $k = k + 1$.

  `Set` $U^n = U^{n,k}$.

on the formulation of the endocardial boundary conditions. The passive parameter values were chosen to provide physiological pressure–volume response over diastole.

5.2. *In vivo* LV models

In order to verify the applicability of the method to *in vivo* data, six models were built using volunteer and patient MR images, following the workflow described in Fig. 4. Specifically, we processed three datasets from healthy volunteers (**V1**–**V3**), and three datasets from patients (**P1**–**P3**) diagnosed with moderate dilated cardiomyopathy (DCM). DCM is associated with LV remodeling, giving the chamber a more spherical shape and higher volume. In addition, deterioration of LV function is observed in DCM. These models provide a diverse set of geometries and modes of function for testing the boundary energy potential terms introduced.

For each case the (non-invasively) acquired images included short-axis and long-axis 2-, 3- and 4-chamber view CINE images, which were then used to create a combined segmentation of the truncated LV at end diastole. An atlas-based meshing strategy [62] was employed for the construction of personalized tetrahedral end-diastolic meshes. Basic mesh characteristics are given in Table 4. In addition, the LV/RV junction region was defined through manual segmentation of end-diastolic short-axis CINE images. The segmentation was used to provide the spatial field H in Eq. (29) on each personalized mesh. Mesh deformations through the cardiac cycle were extracted from 3D tagged MRI using a non-rigid registration algorithm [27] implemented in Image Registration Toolkit.[3]

All simulations used the end-systolic (corresponding to the lowest cavity volume) mesh configuration as the reference state, as discussed in [10]. The volume curve for each case was computed from the data using Eq. (23).

Patient-specific parameters for the constitutive laws were obtained following the estimation procedure described in [10], based on the best match between the data and the model results. First, in passive parameter estimation we minimized the relative total displacement error (over the whole LV and all diastolic frames):

$$\mathcal{J}_p = \left(\frac{\sum_{n=m}^{N} \|\boldsymbol{u}(t_n) - \boldsymbol{u}_d(t_n)\|^2\ dt}{\sum_{n=m}^{N} \|\boldsymbol{u}_d(t_n)\|^2\ dt} \right)^{1/2}, \tag{34}$$

with m and N denoting the end-systolic and end-diastolic time frames respectively. In order to obtain a personalized active tension curve we also relied on patient-specific LV cavity pressure $\lambda_{l,d}(t)$ through the cycle, obtained from the normalized curve in [63], and scaled using the E/E_a estimate for the end-diastolic pressure [53] and the peak

[3] http://www.doc.ic.ac.uk/~dr/software.

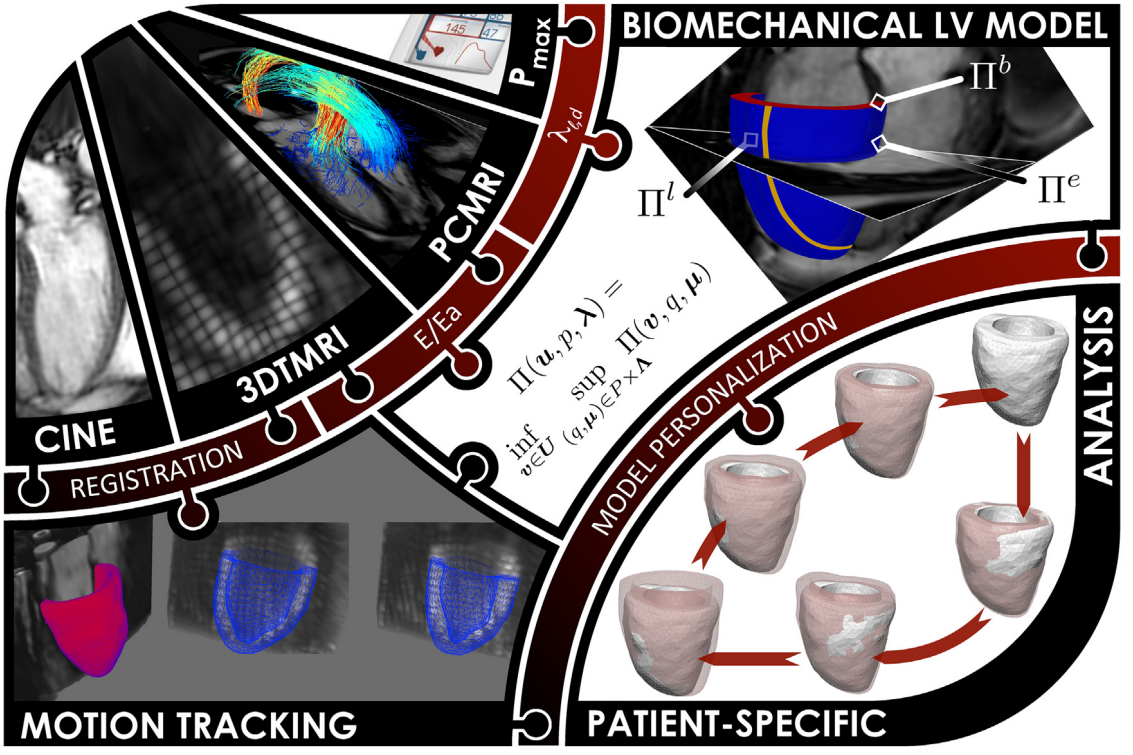

Fig. 4. Workflow followed for the development of patient-specific models. CINE, 3D tagged MRI (TMRI), phase contrast MRI (PCMRI) and CENTRON estimated pressure comprise the key sources of data used in the computational model. CINE and TMRI images were registered enabling construction of the anatomical model and subsequent motion tracking. PCMRI and TMRI were combined to estimate the E/Ea ratio and subsequently estimated end diastolic blood pressure. CENTRON estimates were used to get peak systolic pressure, which was subsequently used to personalize the normalized end diastolic pressure $\lambda_{l,d}$. Pressure estimates along with motion estimation (and motion derived volumes) were incorporated into the model through the epicardial boundary condition (BC), moments + relaxed-base BC and endocardial volume BC. Parametrization was performed by minimizing the difference between the model and data-derived displacements and cavity pressures, producing the final patient-specific model.

systolic pressure value obtained non-invasively using the CENTRON device.[4] Accuracy of the CENTRON estimate compared to invasive central systolic pressure measures was reported to have a standard deviation of 5.9 mmHg [21], constituting an error below 10%. Investigating the impact on the activation parameter α, we observed the maximum value of α changed $\pm 10.3\%$ when the peak CENTRON estimate was modulated by $\pm 10\%$.

At each time frame t_n the value of the active tension $\alpha(t_n)$ was computed as the minimizer of the combined relative displacement and cavity pressure error functional:

$$\mathcal{J}_a(t_n) = 0.5 \frac{\|\boldsymbol{u}(t_n) - \boldsymbol{u}_d(t_n)\|}{\|\boldsymbol{u}_d(t_n)\|} + 0.5 \frac{|\lambda_l(t_n) - \lambda_{l,d}(t_n)|}{|\lambda_{l,d}(t_n)|}. \tag{35}$$

In addition to providing the basis for model personalization, the error functionals $\mathcal{J}_p$ and $\mathcal{J}_a$ allow quantification of the accuracy of the model results over the whole truncated LV.

For a detailed description of the acquired data, image processing pipeline and the specifics of the estimation process, as well as the reasoning behind it we refer to previous work [37,10].

6. Analysis of base plane conditions

Truncation of the heart geometry near the base plane is often applied in the literature [13,4,8,64]. As mentioned in Section 3.1, this leads to an artificial surface over which some boundary condition must be applied. To assess the

[4] http://www.centrondiagnostics.com.

Please cite this article in press as: L. Asner, et al., Patient-specific modeling for left ventricular mechanics using data-driven boundary energies, Comput. Methods Appl. Mech. Engrg. (2016), http://dx.doi.org/10.1016/j.cma.2016.08.002

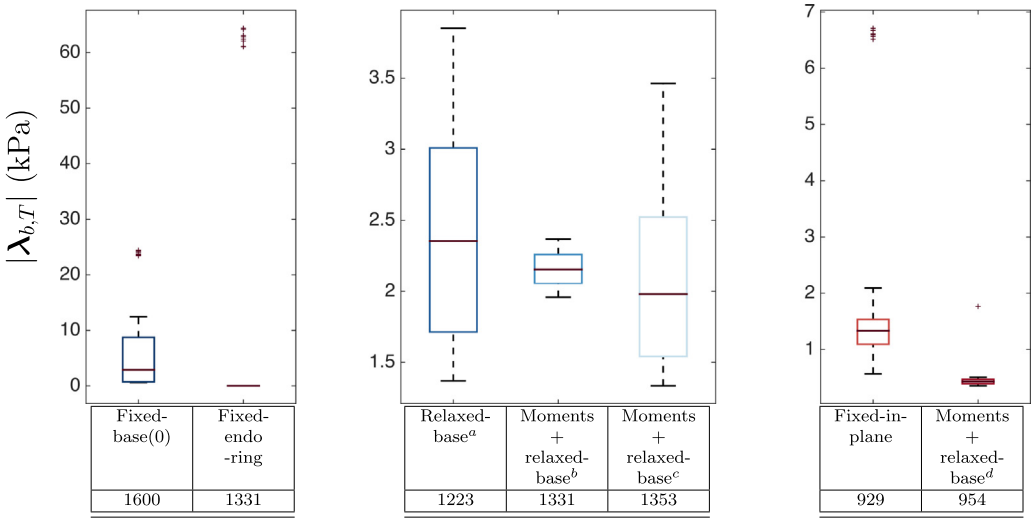

Fig. 5. Boxplot of the base plane traction force magnitudes $|\boldsymbol{\lambda}_{b,T}|$ at node points for different base plane boundary conditions showing the mean, standard deviation and outliers. Each simulation was inflated from reference volume to double the reference volume, with the table below each boxplot providing the corresponding lv lumen pressure λ_l. $^a(\varepsilon_{la}, \varepsilon_{sa}) = 10^{-6}$ using displacements $\boldsymbol{u}_d = 0$ as data, $^b(\varepsilon_{la}, \varepsilon_{sa}) = 0$ using no penalty variable, $^c(\varepsilon_{la}, \varepsilon_{sa}) = 10^{-6}$, and $^d(\varepsilon_{la}, \varepsilon_{sa}) = 10^{-6}$ using the fixed-in-plane displacements as data $\boldsymbol{u}_d$.

common base plane conditions, outlined in Table 1, an idealized heart model was passively inflated to an end diastolic volume (EDV). $\mathcal{A}_t^b$ was selected based on the applied condition as discussed in Section 3.1. Inflation was driven by volume and no epicardial conditions were applied. For comparison, data on the base was assumed $\boldsymbol{u}_d = \mathbf{0}$ except in comparisons with the *fix-in-plane* approach.

Fig. 5 illustrates the applied base plane tractions and the applied endocardial pressure. *Fixed-base(0)* required the highest average boundary tractions as well as larger endocardial inflation pressures to achieve EDV, followed closely by *fixed-endo-ring* which has the highest individual values but lower average. *Relaxed-base* conditions using $(\varepsilon_{la}, \varepsilon_{sa}) = (10^{-6}, 10^{-6})$ produced a reduction in forces and endocardial pressure. This was also observed in the pure *moments* $(\varepsilon_{la}, \varepsilon_{sa}) = (0, 0)$ and *moments* + *relaxed-base* $(\varepsilon_{la}, \varepsilon_{sa}) = (10^{-6}, 10^{-6})$ conditions, which exhibited a reduced range of forces. Interestingly, the endocardial inflation pressures increased partially, however, this can be explained by the increased freedom allowing more in-plane dilation.

The *fixed-in-plane* condition produced the lowest forces and endocardial filling pressures, though still producing a significant range in tractions due to the requirement of planarity. This was expected as the condition does not restrict short-axis motion. Using the general dilation observed as a template for motion ($\boldsymbol{u}_d$), *moments* + *relaxed-base* were further able to reduce the boundary energies and tighten the range of observed forces. We note that this examination cannot confirm which models are more or less correct, as each prescribes conditions using different assumptions. However, it does underscore the significance this condition can have in assessing the mechanics of the heart. In particular, these boundary tractions directly reflect the impact of these assumptions on tissue stresses, including fiber stress which is often a quantity of interest in modeling studies.

To provide insight into base plane motion, tracking data $\boldsymbol{u}_d$ extracted from the images was analyzed in all of the *in vivo* cases (see Fig. 6). Significant motion was observed in the long-axis direction across both patients and volunteers ($E[U_{la}] \pm \sigma(U_{la}) = 10.14 \pm 0.66$ mm). Motion was not only translatory. Stretch was also significant in the plane in volunteers $E[\ell/\ell_0] \pm \sigma(\ell/\ell_0) = 1.53 \pm 0.08$ and in patients $E[\ell/\ell_0] \pm \sigma(\ell/\ell_0) = 1.40 \pm 0.04$. These results indicate that non-trivial motion is present and must be integrated with the LV mechanical model.

Based on the observed motion, *fixed-base(**u**)*, *relaxed-base* and *moments* + *relaxed-base* all provide viable approaches to encapsulate base plane motion into the model. As both *relaxed-base* and *moments* + *relaxed-base* approach *fixed-base(**u**)* as $(\varepsilon_{la}, \varepsilon_{sa}) \to (0, 0)$, we focus our attention on comparing these two methods for a range of $(\varepsilon_{la}, \varepsilon_{sa})$ parameters. Table 5 presents relative error between model displacement and data for the two approaches as well as measures of the total boundary traction for different parameter values. In this case, the diastolic phase (inflating the heart from its end-systolic reference) for **V1** was simulated for varying penalty parameters. $\mathcal{A}_t^b$ was selected based

Please cite this article in press as: L. Asner, et al., Patient-specific modeling for left ventricular mechanics using data-driven boundary energies, Comput. Methods Appl. Mech. Engrg. (2016), http://dx.doi.org/10.1016/j.cma.2016.08.002

	V1	V2	V3	P1	P2	P3
$\lvert\theta\rvert$	1.45	0.00	5.15	0.00	5.56	2.1
$\Delta A/A_0$	7.14	14.94	12.97	3.72	1.99	7.82
U_{la}	10.17	10.80	10.81	9.14	10.28	9.616
ℓ/ℓ_0	1.54	1.44	1.6	1.37	1.38	1.44

Fig. 6. Illustration of motion from ES to ED across patients/volunteers as well as quantitative measures of base plane motion. $|\theta|$ is the angular rotation of the base plane, computed from the complex conjugate eigenvalues of $\widetilde{\mathbf{F}} = \boldsymbol{A} + \boldsymbol{I}$, where $\boldsymbol{A}$ is the best fit affine transformation found by analyzing the moments $\{0,0\}$, $\{1,0\}$, $\{0,1\}$. $\Delta A/A_0 = |A_{ED} - A_{ES}|/A_{ES}$ denotes the relative difference in area scaled by the reference. $U_{la} = \boldsymbol{u}_d \cdot \mathbf{n}_b$ denotes the displacement in the base normal direction. ℓ/ℓ_0 denotes the base plane stretch computed as the maximum eigenvalue of $\widetilde{\mathbf{C}} = \widetilde{\mathbf{F}}^T\widetilde{\mathbf{F}}$.

Table 5
(Left) $L^2(\Gamma_0^b)$ norm difference between simulation ($\boldsymbol{u}^r$)/experiment ($\boldsymbol{u}_d$) using relaxed-base conditions relative to simulation ($\boldsymbol{u}^{mr}$)/experiment ($\boldsymbol{u}_d$) difference using moments and relaxation conditions (for **V1**). Relative norms are provided over a range of long-axis (ε_{la}) and short-axis (ε_{sa}) relaxation parameters. (Right) $L^2(\Gamma_0^b)$ norm of the total base boundary traction ($\boldsymbol{\lambda}_{b,T}^r$) for relaxed ($X = r$) and moments and relaxed ($X = mr$) conditions for equal relaxation parameters.

$\lVert\boldsymbol{u}^r - \boldsymbol{u}_d\rVert_{0,\Gamma_b^0}/\lVert\boldsymbol{u}^{mr} - \boldsymbol{u}_d\rVert_{0,\Gamma_b^0}$							$\lVert\boldsymbol{\lambda}_{b,T}^X\rVert_{0,\Gamma_0^b}\lvert\Gamma_0^b\rvert^{-1/2}$		
$\varepsilon_{sa} \setminus \varepsilon_{la}$	10^{-3}	10^{-4}	10^{-5}	10^{-6}	10^{-7}	10^{-8}	$\varepsilon_{sa}, \varepsilon_{la}$	r	mr
10^{-3}	–	–	3.45	1.57	1.52	1.52	10^{-3}	–	530
10^{-4}	–	13.06	3.43	1.50	1.45	1.45	10^{-4}	155	531
10^{-5}	18.51	11.90	3.73	1.28	1.19	1.18	10^{-5}	384	553
10^{-6}	23.27	17.22	6.22	1.54	1.05	1.04	10^{-6}	712	750
10^{-7}	26.90	20.56	8.12	2.65	1.22	1.02	10^{-7}	1050	1056
10^{-8}	26.77	20.61	8.19	2.73	1.61	1.09	10^{-8}	1557	1558

on the applied condition as discussed in Section 3.1. Inflation was driven by volume and epicardial conditions were applied.

From Table 5, we observe that as $(\varepsilon_{la}, \varepsilon_{sa}) \to (0,0)$ the relative performance of *relaxed-base* and *moments + relaxed-base* approaches converge (relative error goes to 1), and the measure of tractions also converge. We note that *moments + relaxed-base* always exhibits lower error and higher traction for a given penalty parameter combination. While low penalty parameters reduce errors between model and data, this comes at the expense of increased boundary traction, which grows by a factor of 3. Moreover, the spatial coherence of the boundary traction is lost (see Fig. 7(E)), giving large (seemingly random) variations in the applied basal traction – likely due to noise in the extracted motion field $\boldsymbol{u}_d$. Using more relaxed (high penalty) values, extremely high errors are observed in the *relaxed-base* condition. These are largely due to ε_{la}, which must be sufficiently low in this approach to avoid large error in the long-axis location of the base plane. This issue is not observed in the *moments + relaxed-base* approach where average errors were always <1.4 mm. *Moments + relaxed-base* thus enables a good match to the data without requiring low penalty parameter values, providing greater robustness to noisy data as well as data that is potentially incomplete or sparse.

To better understand the behavior of the introduced *moments + relaxed-base* constraint, Fig. 7 shows the errors for different penalty values along with plots of the boundary traction magnitude for equal $\varepsilon_{la}, \varepsilon_{sa}$. As mentioned, errors remain below 1.4 mm for all parameters. Observing the trend as the penalty parameters are reduced, we see both amplification and incoherence of the boundary traction. Additionally, maximal traction forces for E–F exceed 50 kPa and are significantly larger than those seen in A–D. For high penalty, we note that the distribution of basal forces is minimal, while in C–D a general transmural trend becomes dominant, which can be explained by the significant transmural variation in myocardial fiber structure.

Please cite this article in press as: L. Asner, et al., Patient-specific modeling for left ventricular mechanics using data-driven boundary energies, Comput. Methods Appl. Mech. Engrg. (2016), http://dx.doi.org/10.1016/j.cma.2016.08.002

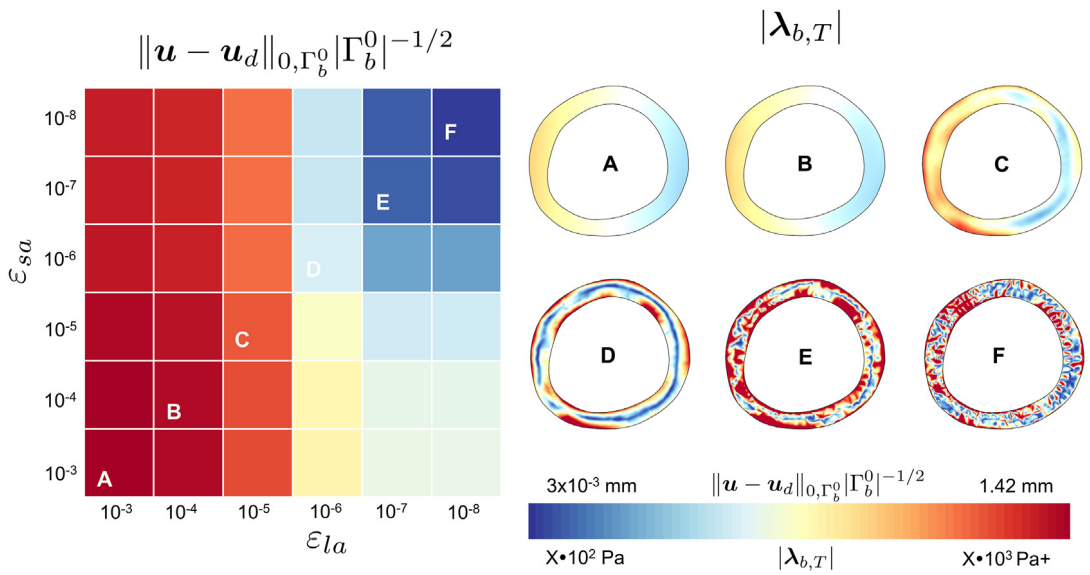

Fig. 7. (Left) Quantification of mean base plane difference between simulation and data for **V1** over a range of long-axis (ε_{la}) and short-axis (ε_{sa}) relaxation parameters. (Right) Magnitude of the total boundary traction ($\boldsymbol{\lambda}_{b,T}$) for combinations of relaxation parameters (A–F) marked in the box plot on the left. A variable magnitude was applied to illustrate boundary tractions with (A–C, $X = 1$), (D–E, $X = 2$), (F, $X = 4$).

Based on these results, $(\varepsilon_{la}, \varepsilon_{sa})$ can be used to balance displacement accuracy while maintaining plausible tractions. We note that the values of $(\varepsilon_{la}, \varepsilon_{sa})$ are relative to the passive stiffness values, which in this case are $\sim\mathcal{O}(10^3)$. This raises interesting questions during the systolic phase, where stiffness increases roughly by two orders of magnitude due to muscle contraction. As the truncation leads to a cut surface through the myocardial muscle, forces across the surface are similarly likely to increase during the systolic phase. Hence, we suggest that $\varepsilon_{la,sa} \approx 10^{-3}/\delta(t)$, with $\delta(t) = \max\{a, a_f, \alpha(t)\}$ giving the rough scaling of the dominant myocardial stresses.

7. Accuracy of endocardial boundary conditions

The endocardial boundary conditions introduced in Section 3.2 and summarized in Table 2 were applied and compared with respect to their accuracy on the *in silico* and *in vivo* model problems presented in Section 5. The methods were compared over passive filling diastolic simulations, whereby the cavity volume of the inflated ventricle was computed and the Lagrange multiplier λ_l provided the intraventricular pressure. The accuracy of the simplified volume inflation (SVI, Eq. (24)), volume rate inflation (VRI, Eq. (26)) and volume inflation (VI, Eq. (28)) boundary conditions was assessed by comparing their volume and pressure outcomes with the ground truth results of the commonly used pressure inflation (PI, Eq. (19)) approach.

The *in silico* tests were used to examine the assumption that the base motion has a negligible effect on cavity volume calculation. Accordingly, passive inflation simulations were performed having a fixed base as well as imposing a 5 mm displacement of the basal plane along the long axis direction. In both cases, a zero traction condition was enforced on the epicardial wall and the base displacement was enforced as a Dirichlet condition.

In the case of the fixed base (Fig. 8) the three approaches behaved in a similar manner, producing equivalent results to the ground truth PI simulation. In fact, the maximum percentage volume and pressure error was less than $10^{-4}\%$ for the VI and SVI methods, while the maximum percentage error in volume and pressure was around 0.1% and 1%, respectively, for the VRI approach. This increase in error in the VRI approach resulted from the temporal discretization which, unlike the other methods, is an additional source of error. In agreement with the definitions of the SVI and VRI approaches which are based on the assumption of negligible basal motion, all methods exhibited consistent behavior over fixed-base inflation simulations. These tests confirmed the equivalence of all approaches under minimal basal motion, allowing their reliable usage for volume calculation in LV models with negligible base motion.

However, when simulations included basal motion the accuracy of the SVI and VRI deteriorated (Fig. 9). Specifically, the error in volume increased to 1.3% and 3.7% for the SVI and VRI respectively. Interestingly, the

Please cite this article in press as: L. Asner, et al., Patient-specific modeling for left ventricular mechanics using data-driven boundary energies, Comput. Methods Appl. Mech. Engrg. (2016), http://dx.doi.org/10.1016/j.cma.2016.08.002

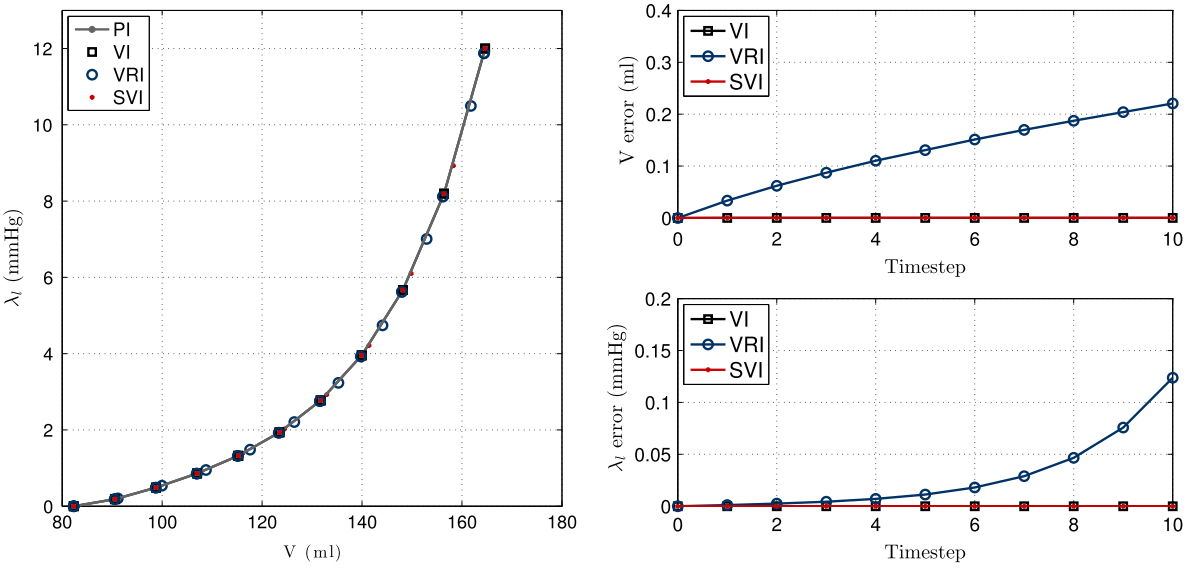

Fig. 8. Comparison of the endocardial boundary conditions over diastolic filling model problem with a fixed base. (Left) Pressure–volume plots of the pressure inflation (PI), simplified volume inflation (SVI), volume rate inflation (VRI), and volume inflation (VI) simulations. Error between (Top right) volume and (Bottom right) pressure (λ_l) of the SVI, VRI, VI and ground truth PI simulations over time.

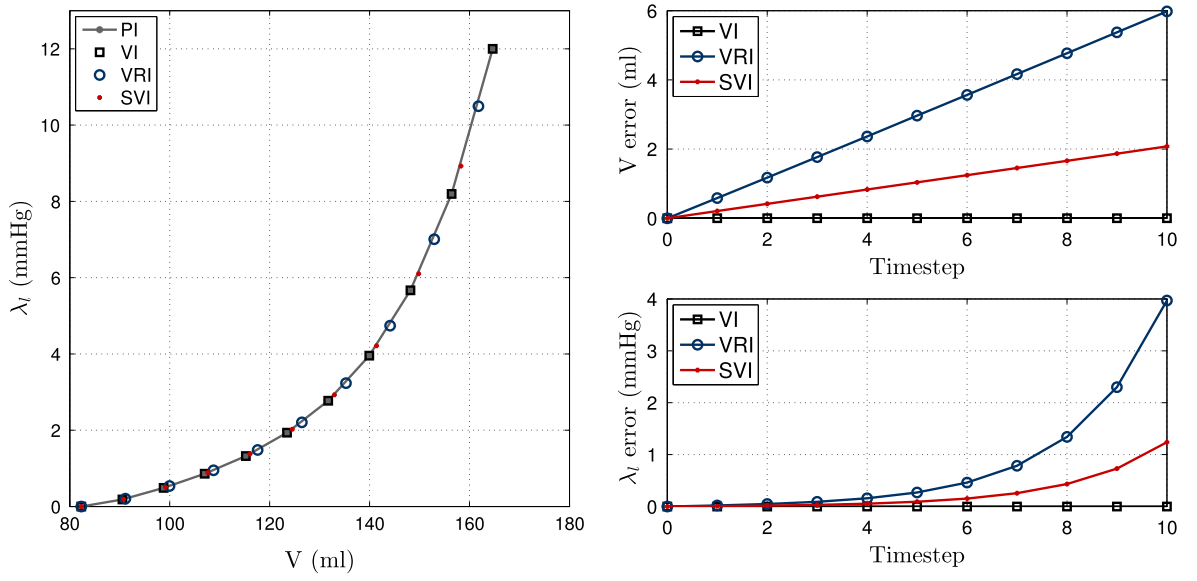

Fig. 9. Comparison of the endocardial boundary conditions over diastolic filling model problem, with the base moving along the long axis direction. (Left) Pressure–volume plots of the pressure inflation (PI), simplified volume inflation (SVI), volume rate inflation (VRI), and volume inflation (VI) simulations. Error between (Top right) volume and (Bottom right) pressure (λ_l) of the SVI, VRI, VI and ground truth PI simulations over time.

effect on pressure was even more pronounced, with errors of 10.3% and 33% for the SVI and VRI boundary conditions respectively. Nevertheless, the accuracy of the VI approach was preserved, producing errors smaller than 10^{-4}% in both volume and pressure. The relatively small basal motion (5 mm) imposed in these tests was adequate to cause a substantial difference in accuracy between the methods. Considering that this motion was modest compared to basal motion observed *in vivo* (Fig. 6), the inaccuracies introduced by the SVI and VRI in pressure and volume are likely to be amplified *in vivo*.

Please cite this article in press as: L. Asner, et al., Patient-specific modeling for left ventricular mechanics using data-driven boundary energies, Comput. Methods Appl. Mech. Engrg. (2016), http://dx.doi.org/10.1016/j.cma.2016.08.002

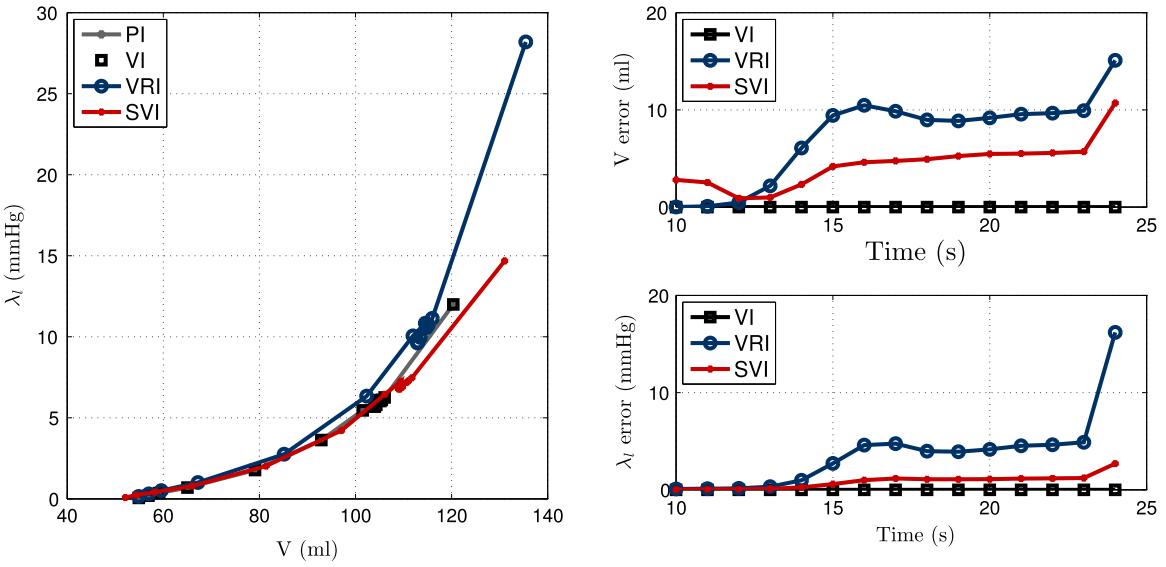

Fig. 10. Accuracy of endocardial boundary conditions in an *in vivo* test using data from **V3**. (Left) Pressure–volume plots of the pressure inflation (PI), simplified volume inflation (SVI), volume rate inflation (VRI), and volume inflation (VI) simulations. Error between (Top right) volume and (Bottom right) pressure (λ_l) of the SVI, VRI, VI and ground truth PI simulations over time.

In order to assess the actual impact of these inaccuracies *in vivo* – where the basal motion is typically not only more substantial but also non-axisymmetric as discussed in Section 6 – the endocardial boundary conditions were applied on a test using *in vivo* data from case **V3** (Section 5.2). Within these simulations the prescribed volume was derived from tracked 3D tagged MRI data and the cavity pressure was assumed to be known. In addition, the base motion was imposed through a relaxed constraint (Eq. (14)) and an RV-epicardial boundary condition (Eq. (29)) was applied.

Based on Fig. 10 the base motion has a significant effect on the LV volume computation, leading the SVI and VRI boundary conditions – which consider this effect to be negligible – to introduce large volume errors (maximum percentage error 7.2% and 12.2%, respectively). Inaccuracies in volumes were also propagated in the intraventricular pressure, with errors of 50% and 93% for the SVI and VRI. It is worth noting the amplification in both volume and pressure errors compared to the *in silico* tests, which likely resulted from incorporating patient-specific geometry and motion as opposed to the idealized geometry and axisymmetric motion in the *in silico* problem.

The *in silico* and *in vivo* tests performed highlight that the base motion has a significant effect on the overall volume calculation, leading to marked volume errors when neglected. In addition, volume errors lead to notable errors in cavity pressure and are also likely to introduce bias in other metrics including stiffness estimates and wall stresses. Considering the substantial base motion (Fig. 6) observed in *in vivo* cases, the VI approach should be taken to ensure accurate cavity volumes and physiological model outcomes.

8. Significance of epicardial boundary conditions

Left-ventricular mechanics models commonly consider an isolated LV, neglecting the effect of the RV on myocardial motion and dynamics, as mentioned in Section 3.3. However, preliminary *in vivo* tests which assumed no epicardial tractions produced relative large displacement errors (Fig. 11). When compared against CINE images, all *in vivo* models exhibited a tendency to shift away from the RV during diastolic filling (representative example in Fig. 11). This consistency in model behavior and deviation from images provided evidence of non-negligible forces acting on the epicardial wall. Although these forces are potentially caused from multiple sources as discussed in Section 3.3, the RV is likely producing a traction on the region of attachment to the LV.

In order to account for the traction the RV is exerting on the LV/RV junction during diastole, the RV epicardial boundary condition in Eq. (29) was employed in *in vivo* diastolic simulations. To assess the significance of considering these forces, diastolic simulations were performed for all cases with and without the RV epicardial boundary condition. Throughout these tests the LV was inflated to the end-diastolic volume using the VI approach and base motion was applied using *moments + relaxed-base* approach.

Please cite this article in press as: L. Asner, et al., Patient-specific modeling for left ventricular mechanics using data-driven boundary energies, Comput. Methods Appl. Mech. Engrg. (2016), http://dx.doi.org/10.1016/j.cma.2016.08.002

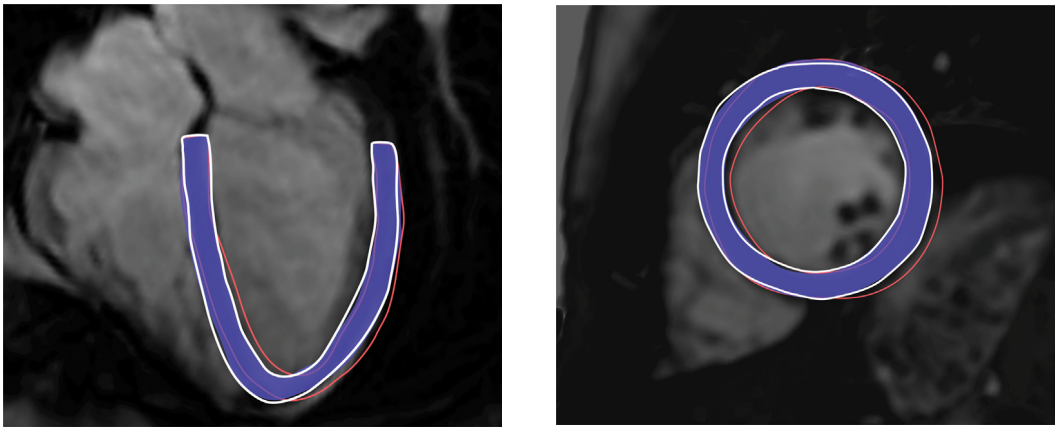

Epicardial boundary conditions

	V1	V2	V3	P1	P2	P3
$\mathcal{J}_p$ (%) w/o RV BC	33	50	51	62	55	36
$\mathcal{J}_p$ (%) w RV BC	22	29	23	33	26	18

Fig. 11. (Top) Tracked (white mesh lines) and simulated end-diastolic state with (blue mesh volume) and without (red mesh lines) an RV epicardial boundary condition (RV BC) for **V3**, in long-axis and short-axis views. (Bottom) Relative total displacement error in diastole $\mathcal{J}_p$ for simulations with and without the RV BC. (For interpretation of the references to color in this figure legend, the reader is referred to the web version of this article.)

Table 6
Relative total errors in diastole and systole for the *in vivo* models, illustrating the accuracy of the simulations as compared to the deformations extracted from 3D tagged images and the pressures based on the scaled empirical curve [63].

	V1	V2	V3	P1	P2	P3
$\mathcal{J}_p$, %	22	29	23	33	26	18
$\min_{\text{systole}} \mathcal{J}_a(t)$, %	11	9	12	16	14	12
$\max_{\text{systole}} \mathcal{J}_a(t)$, %	19	17	19	21	18	13

Based on the notable reduction in relative displacement errors in Fig. 11 (the average error decreased from approximately 48% to 25%) we can deduce the significant improvement in model accuracy when the RV forces are considered. Direct comparisons of simulated results on CINE MRI images (Fig. 11) suggest that the forces exerted on the LV/RV junction when employing the RV epicardial boundary condition restrict the simulated deformation on a more anatomically accurate position in space, leading to the substantial reduction in model error observed.

The proposed epicardial boundary condition is relatively easy to impose, not requiring additional data or introducing further assumptions about the RV function or other organs, yet it is capable of reducing model errors to approximately half of the original values.

9. Patient-specific full-cycle simulations using *in vivo* data

As a verification of the model's utility applied to *in vivo* data, we simulated the full cardiac cycle for six volunteer and patient cases. The boundary conditions were chosen so that a good combination of accuracy in displacements and physiological pressures in the tissue was achieved. Specifically, the *moments* + *relaxed*-base condition with $(\varepsilon_{la}, \varepsilon_{sa}) = (10^{-6}, 10^{-6})$ in the passive stage were applied on Γ_0^b, the volume inflation based on V_{VI} was prescribed on Γ_0^l, and the epicardial condition was used with $\varepsilon_e = 5 \cdot 10^{-6}$ in the passive stage. The values of the relaxation parameters were scaled consistently with the active tension, as suggested in Section 6: $\varepsilon_{la} = \varepsilon_{sa} = 10^{-3}/\delta(t)$ and $\varepsilon_e = 5 \cdot 10^{-3}/\delta(t)$, where $\delta(t) = \max\{10^3, \alpha(t)\}$. The results were obtained using the passive parameters and active tension curves presented in Fig. 12.

Please cite this article in press as: L. Asner, et al., Patient-specific modeling for left ventricular mechanics using data-driven boundary energies, Comput. Methods Appl. Mech. Engrg. (2016), http://dx.doi.org/10.1016/j.cma.2016.08.002

	IM	V1	V2	V3	P1	P2	P3
a, Pa	44	268	240	200	1057	1173	857
a_f, Pa	1744	2680	1715	1111	5872	2608	6593
$\hat{\alpha}$, kPa	-	112	121	108	116	154	163
$\hat{\tau}$, s	-	0.22	0.19	0.20	0.28	0.24	0.28

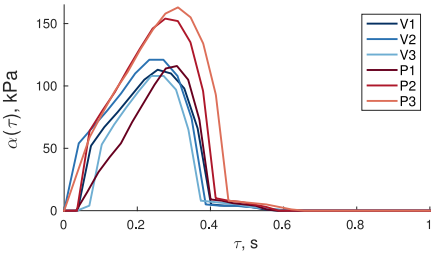

Fig. 12. Patient-specific inputs for the idealized (**IM**) and the *in vivo* models, obtained from minimizing total relative errors between the data and the model. (Left) Numeric values for passive and active parameters: a and a_f are the isotropic and the fiber stiffnesses in the passive constitutive law, $\hat{\alpha} = \max_t \alpha(t)$ is the peak active tension, and $\hat{\tau} = \arg\max \alpha(t) \cdot HR/60$ is the normalized time in the cycle where this peak is achieved, HR being the heart rate in a given case. The remaining parameters of the reduced Holzapfel–Ogden law $b = b_f = 5.0$ were chosen to match empirical data on diastolic pressure–volume behavior [37]. (Right) Full-cycle patient-specific active tension curves $\alpha(\tau)$ linearly interpolated between the image frames available. All cycles are normalized to 1 s duration with $\tau = t \cdot HR/60$. (For interpretation of the references to color in this figure legend, the reader is referred to the web version of this article.)

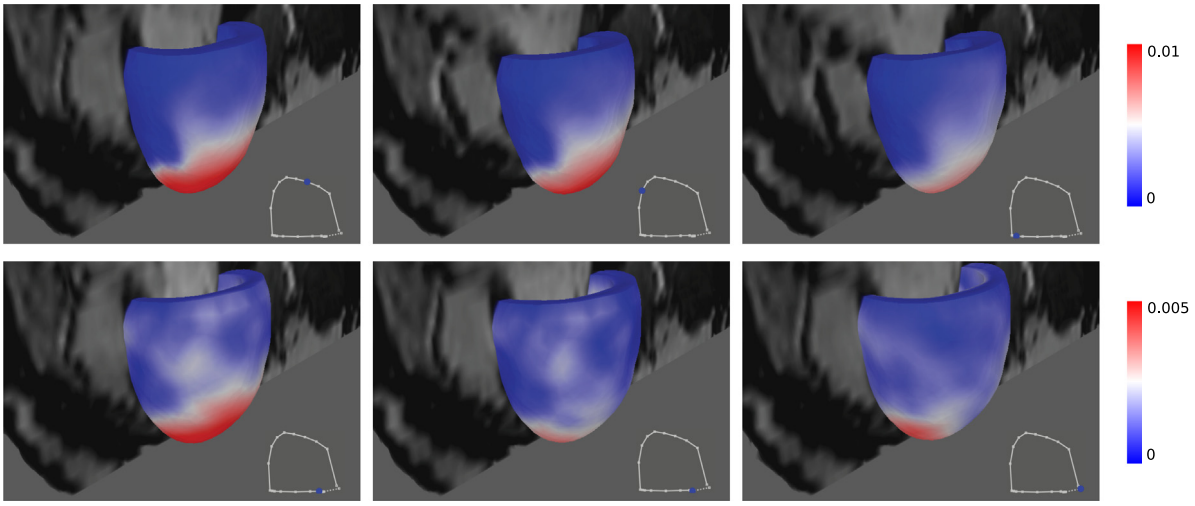

Fig. 13. Illustration of simulated deformation over the cardiac cycle for **V3**. Mesh volume is colored based on the magnitude of the displacement error which is given in meters. The blue circle on the PV loop in each image corresponds to the presented cardiac phase. (For interpretation of the references to color in this figure legend, the reader is referred to the web version of this article.)

Mesh deformations over the full cycle are shown together with short-axis cine images for one of the cases, **V3**, in Fig. 13. The values of the relative error functionals for all cases are given in Table 6, with diastolic metrics varying around 20%–30%, and systolic metrics around 10%–20%. In Fig. 14 we compare the pressure–volume loops extracted from the data to those obtained from the simulations.

In addition to qualitative assessment of the results, such as that provided by a specific cut plane in Fig. 11, the proposed approach allows a meaningful direct comparison between the data and the simulation results over the whole of the truncated LV domain. The boundary conditions ensure that the motion of the model is not simplified to the extent that it can no longer be related to patient data: *e.g.* the base plane does not remain stationary and cut through the ventricle or the atrium, and the ventricle does not relax away from the RV and outside the pericardium. The one-to-one comparison that we perform is not commonly seen in modeling results, but its wider use would provide a quantitative measure of model accuracy which can serve as basis for comparison between cases and inform model selection process.

An important feature of the proposed model is its robustness to the data. Figs. 6 and 14 illustrate some of the variability observed *in vivo*: even within the cohorts (healthy volunteers vs DCM patients) the differences can be dramatic. These are often overlooked in idealized models, and some of the challenges simply do not arise before multiple real cases are processed. As an example, subjects **V2** and **P1** do not exhibit any rotation of the base between end systole and

Please cite this article in press as: L. Asner, et al., Patient-specific modeling for left ventricular mechanics using data-driven boundary energies, Comput. Methods Appl. Mech. Engrg. (2016), http://dx.doi.org/10.1016/j.cma.2016.08.002

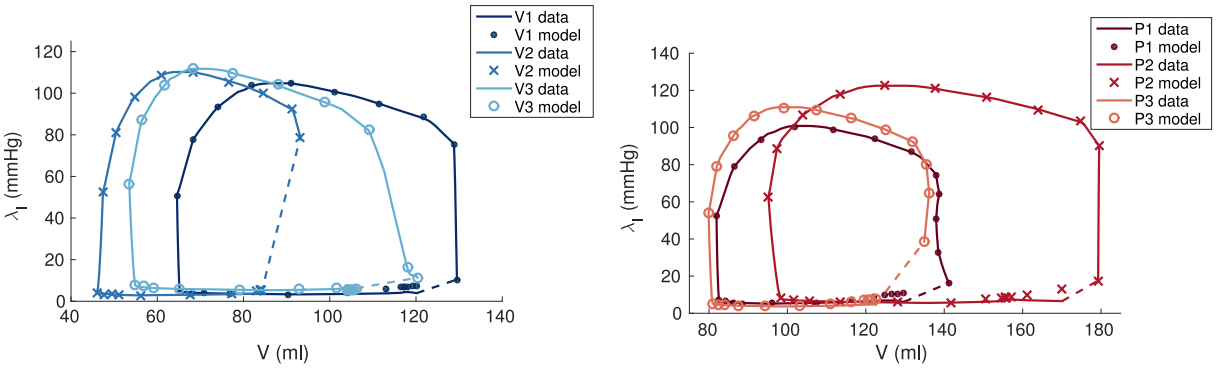

(a) Volunteers.

(b) Patients.

Fig. 14. (LV cavity) pressure–volume loops for the *in vivo* models illustrating model behavior over most of the duration of the cardiac cycle. The data is represented by solid lines—the loops are not complete due to the fact that (prospectively ECG triggered) 3D tagged images usually do not cover the whole cardiac cycle. The dashed lines connect the last and the first available data points.

end diastole, but disallowing it in the model would introduce a bias in simulation results for **V3** and **P2**. The range of cavity volumes and cardiac outputs (differences between end-diastolic and end-systolic volumes) as well as anatomical features such as wall thickness and ventricle shape (which is significantly different in DCM compared to health) have a strong effect on simulation results and performance, as well as the errors $\mathcal{J}_a$ and $\mathcal{J}_p$. Our ability to produce consistently operational models for all of these cases is an important step in taking modeling further towards translation.

These results illustrate the capacity to develop high-fidelity computational models with dynamics that closely follow the motion observed from medical images. The result is a *diagnostic* model, capable of providing or inferring a link between observed motion and the kinetics active in a patients heart. Quantities such as stiffness, active contraction and work – all of which have potential clinical significance – can be quantified from such models. Another important scope is for *prognostic* models which not only characterize what is, but provide an estimate of what will be. Specifically, prognostic models are desirable in the process of therapy planning and device assessment. Beyond requiring a model with sufficient robustness to provide some predictive insight, prognostic models have the added challenge of requiring appropriate boundary conditions that can adapt to reflect the change in function observed in the heart. While acute changes may be more closely related to observed motion characteristics, these may be inappropriate long-term. For example, prescribing transient LV lumen volume may be inappropriate when considering therapy response. Use of Windkessel models (for example in [8]) addresses this by allowing for adaptability in the predicted volumetric transient. However, these predictions are often acute and may neglect cardiovascular regulatory mechanisms necessary for gauging long-term response. Proper development and assessment of predictive boundary conditions remains an important and only partially addressed challenge.

10. Conclusions

This work investigates the role of boundary conditions in personalized models of left-ventricular mechanics and introduces new data-driven boundary energy terms. The proposed boundary conditions are devised so that accuracy of simulation results as compared to the data is balanced with coherence in tractions on the surfaces of the myocardium. The evaluation of the boundary conditions is performed using an idealized *in silico* model as well as six *in vivo* models of healthy and diseased hearts. The use of data-derived motion in prescribing base and epicardial conditions allows a significant improvement in model accuracy, while relaxation needs to be applied to prevent the associated forces from becoming non-physiological. Endocardial conditions are shown to be sensitive to the assumptions regarding base motion, which need to be considered in the context of realistic cardiac behavior. *In vivo*, model fidelity is assessed via L_2-norms of displacement errors between simulation results and data from non-invasive imaging. Full-cycle simulations of the *in vivo* cases that employ the model with the proposed boundary conditions show quantitative behavior observed in the data, and account for non-trivial differences between cases due to anatomy, motion and function.

Please cite this article in press as: L. Asner, et al., Patient-specific modeling for left ventricular mechanics using data-driven boundary energies, Comput. Methods Appl. Mech. Engrg. (2016), http://dx.doi.org/10.1016/j.cma.2016.08.002

Acknowledgments

Authors acknowledge funding from the BHF New Horizons program (NH/11/5/29058), the Engineering and Physical Sciences Research Council (EP/N011554/1), and support from the Wellcome Trust EPSRC Centre of Excellence in Medical Engineering (WT 088641/Z/09/Z) and the NIHR Biomedical Research Centre at Guy's and St.Thomas' NHS Foundation Trust and KCL. The views expressed are those of the authors and not necessarily those of the NHS, the NIHR, or the DoH. Authors also thank Dr. Eric Kerfoot for his help with visualization.

Appendix A. Function spaces for the cardiac mechanical system

In this section, we briefly outline the spaces used for describing the variables used in the energy potential minimization as well as the FEM weak form. $\boldsymbol{U}$ and P denote the space of admissible displacement and pressure solutions at any instant in time $t \in [0, T]$ ensuring the internal energy potential $\Pi_t^{int} : \boldsymbol{U} \times P \to \mathbb{R}$ (at each point in time $t \in [0, T]$) and its directional derivatives are bounded. Considering the internal energy potential defined in Eq. (5), we see that

$$\Pi_t^{int}(\boldsymbol{v}, q) \leq \|\psi(\boldsymbol{F}_{\boldsymbol{v}}, t)\|_{0,1} + \|q\|_{0,2}\left(\|J_{\boldsymbol{v}}\|_{0,2} + |\Omega|^{1/2}\right),$$

while the directional derivative w.r.to $\mathcal{D}_{(\boldsymbol{u},p)}$ can be bounded by,

$$\mathcal{A}_t(\boldsymbol{u}, p; \boldsymbol{v}, q) \leq \left(\|\nabla_{\boldsymbol{F}}\psi(\boldsymbol{F}_{\boldsymbol{u}}, \mathbf{X}, t)\|_{0,2} + 3\|p\|_{0,2}\|\nabla_{\boldsymbol{F}} J_{\boldsymbol{u}}\|_{0,4}\right)\|\boldsymbol{v}\|_{1,4} + \left(\|J_{\boldsymbol{u}}\|_{0,2} + |\Omega|^{1/2}\right)\|q\|_{0,2}.$$

Hence, we can write the general space of admissible solutions $\boldsymbol{U}$ and P (at each point in time $t \in [0, T]$),

$$\boldsymbol{U} = \left\{\boldsymbol{v} \in \boldsymbol{W}^{1,4}(\Omega_0) \,\middle|\, \psi \in L^1(\Omega_0),\ \nabla_{\boldsymbol{F}}\psi \in [L^2(\Omega_0)]^{3\times 3},\ J_{\boldsymbol{v}} \in L^2(\Omega_0),\ \nabla_{\boldsymbol{F}} J_{\boldsymbol{v}} \in [L^4(\Omega_0)]^{3\times 3}\right\}$$
$$P = L^2(\Omega_0)$$

with $\boldsymbol{W}^{1,4}(\Omega_0) = [W^{1,4}(\Omega_0)]^3$ and $L^p(\Omega_0)$ denoting the usual Sobolev and Banach spaces, respectively [70]. The final space $\boldsymbol{U}$ depends on the form of the strain energy function ψ, which is often nonlinearly dependent on the deformation gradient (itself linearly dependent on the displacement gradient).

It remains only to verify that $\boldsymbol{U}$ is sufficient for the boundary terms and to identify the associated spaces for our Lagrange multipliers and penalty variables. Considering the introduced boundary energy terms, Lagrange multipliers in Eqs. (18), (22), (30) are largely simple scalar or vectors which are constant over their respective boundaries. We note that here we assume the area weighted normal $\tilde{\mathbf{n}}$ in Eq. (23) are given data in $\boldsymbol{L}^2(\Gamma_0^l)$.

The exceptions occur with both $\boldsymbol{\lambda}_b$ and $\boldsymbol{\lambda}_e$ which provide more complex, spatially varying boundary forces. In both of these cases, the boundary multipliers must be in $\boldsymbol{L}^2(\Gamma_0^k)$ restricted to their boundaries ($k = b$ or e) owing to the penalty formulations seen in Eqs. (18) and (30). In this case,

$$\begin{aligned}
\Pi_t^b(\boldsymbol{v}, \{\boldsymbol{\mu}_b\}) &= \sum_m \boldsymbol{\mu}_b^m \cdot M_m[\boldsymbol{v} - \boldsymbol{u}_d(t)] + \int_{\Gamma_0^b} \boldsymbol{\mu}_b \cdot \left(\boldsymbol{v} - \boldsymbol{u}_d - \frac{1}{2}\boldsymbol{\Sigma}\boldsymbol{\mu}_b\right)\, d\boldsymbol{X} \\
&\leq \left(\sum_m C_b^m |\boldsymbol{\mu}_b^m| + \|\boldsymbol{\mu}_b\|_{0,\Gamma_0^b}\right)\left(\|\boldsymbol{v}\|_{0,\Gamma_0^b} + \|\boldsymbol{u}_d(t)\|_{0,\Gamma_0^b}\right) + C_b\|\boldsymbol{\mu}_b\|^2_{0,\Gamma_0^b} \\
\Pi_t^e(\boldsymbol{v}, \boldsymbol{\mu}_e) &= \int_{\Gamma_0^e} H\boldsymbol{\mu}_e \cdot \left(\boldsymbol{v} - \boldsymbol{u}_d(t) - \frac{\varepsilon_e}{2}\boldsymbol{\mu}_e\right)\, d\boldsymbol{X} \\
&\leq \|\boldsymbol{\mu}_e\|_{0,\Gamma_0^e}\left(\|\boldsymbol{v}\|_{0,\Gamma_0^e} + \|\boldsymbol{u}_d(t)\|_{0,\Gamma_0^e}\right) + \frac{\varepsilon_e}{2}\|\boldsymbol{\mu}_e\|^2_{0,\Gamma_0^b}
\end{aligned}$$

with $C_b^m = |M_m[\omega^m]|^{1/2}$ (for $m = \{0,0\}, \{1,0\}, \{0,1\}$) being the norm of different moment weights and $C_b = \frac{1}{2}\max(\varepsilon_{la}, \varepsilon_{sa})$ being half the maximum eigenvalue of the penalty matrix $\boldsymbol{\Sigma}$. Owing to the Trace theorem, boundedness of these boundary terms is ensured by the space $\boldsymbol{U}$ (which is more regular). A similar inequality can be derived for $\mathcal{A}_t^b$ and $\mathcal{A}_t^e$ yielding the same restrictions on the smoothness of $\boldsymbol{U}$.

Please cite this article in press as: L. Asner, et al., Patient-specific modeling for left ventricular mechanics using data-driven boundary energies, Comput. Methods Appl. Mech. Engrg. (2016), http://dx.doi.org/10.1016/j.cma.2016.08.002

For ease, in this paper we have assumed that the spaces of $\boldsymbol{\lambda}_b$ and $\boldsymbol{\lambda}_e$ are actually smoother. This is sensible in the case of $\boldsymbol{\lambda}_b$ as the boundary is actually a cut through the myocardium itself. Similarly, the epicardial boundary is also cut along the LV/RV junction though this can be modeled as discontinuous moving from the junction to the septal boundary or epicardium. Here, however, we have assumed that as smooth gradation in the traction is present. As a result, we take both variables from their respective trace spaces, *i.e.*

$$\gamma_k \boldsymbol{U} = \{\boldsymbol{\mu}_k \in \boldsymbol{L}^2(\Gamma_0^k) | \boldsymbol{\mu}_k = \boldsymbol{v} \ \text{ on } \Gamma_0^k, \ \text{for some } \boldsymbol{v} \in \boldsymbol{U}\}.$$

Extending these spaces into the discrete setting of Section 4, the finite element approximation spaces $\boldsymbol{U}^h$ and $\boldsymbol{P}^h$ are built in the usual way. Similarly, the trace spaces are designed by selecting representative functions from the boundaries spaces of $\boldsymbol{U}^h$.

References

[1] R. Chabiniok, V.Y. Wang, M. Hadjicharalambous, L. Asner, J. Lee, M. Sermesant, E. Kuhl, A.A. Young, P. Moireau, M.P. Nash, et al., Multiphysics and multiscale modelling, data–model fusion and integration of organ physiology in the clinic: ventricular cardiac mechanics, Interface Focus 6 (2) (2016) 20150083.
[2] A. Lopez-Perez, R. Sebastian, J.M. Ferrero, Three-dimensional cardiac computational modelling: methods, features and applications, Biomed. Eng. 14 (1) (2015) 35. online.
[3] N.A. Trayanova, Whole-heart modeling applications to cardiac electrophysiology and electromechanics, Circ. Res. 108 (1) (2011) 113–128.
[4] M.P. Nash, P.J. Hunter, Computational mechanics of the heart, J. Elasticity 61 (1–3) (2001) 113–141.
[5] M. Sermesant, P. Moireau, O. Camara, J. Sainte-Marie, R. Andriantsimiavona, R. Cimrman, D.L. Hill, D. Chapelle, R. Razavi, Cardiac function estimation from MRI using a heart model and data assimilation: advances and difficulties, Med. Image Anal. 10 (4) (2006) 642–656.
[6] V.Y. Wang, H. Lam, D.B. Ennis, B.R. Cowan, A.A. Young, M.P. Nash, Modelling passive diastolic mechanics with quantitative MRI of cardiac structure and function, Med. Image Anal. 13 (5) (2009) 773–784.
[7] S. Göktepe, E. Kuhl, Electromechanics of the heart: a unified approach to the strongly coupled excitation–contraction problem, Comput. Mech. 45 (2–3) (2010) 227–243.
[8] A. Krishnamurthy, C.T. Villongco, J. Chuang, L.R. Frank, V. Nigam, E. Belezzuoli, P. Stark, D.E. Krummen, S. Narayan, J.H. Omens, A.D. McCulloch, R.C.P. Kerckhoffs, Patient-specific models of cardiac biomechanics, J. Comput. Phys. 244 (2013) 4–21.
[9] M. Genet, L.C. Lee, B. Baillargeon, J.M. Guccione, E. Kuhl, Modeling pathologies of systolic and diastolic heart failure, Ann. Biomed. Eng. (2015) http://dx.doi.org/10.1007/s10439–015–1351–2.
[10] L. Asner, M. Hadjicharalambous, R. Chabiniok, D. Peresutti, E. Sammut, J. Wong, G. Carr-White, P. Chowienczyk, J. Lee, A. King, N. Smith, R. Razavi, D. Nordsletten, Estimation of passive and active properties in the human heart using 3D tagged MRI, Biomech. Model. Mechanobiol. (2015) 1–19.
[11] S. Dokos, B.H. Smaill, A.A. Young, I.J. LeGrice, Shear properties of passive ventricular myocardium, Am. J. Physiol.-Heart Circ. Physiol. 283 (6) (2002) H2650–H2659.
[12] J.M. Guccione, K.D. Costa, A.D. McCulloch, Finite element stress analysis of left ventricular mechanics in the beating dog heart, J. Biomech. 28 (10) (1995) 1167–1177.
[13] G.A. Holzapfel, R.W. Ogden, Constitutive modelling of passive myocardium: a structurally based framework for material characterization., Phil. Trans. R. Soc. A 367 (1902) (2009) 3445–3475.
[14] G. Sommer, A.J. Schriefl, M. Andrä, M. Sacherer, C. Viertler, H. Wolinski, G.A. Holzapfel, Biomechanical properties and microstructure of human ventricular myocardium, Acta biomaterialia 24 (2015) 172–192.
[15] P. Nielsen, I. Le Grice, B. Smaill, P. Hunter, Mathematical model of geometry and fibrous structure of the heart, American Journal of Physiology-Heart and Circulatory Physiology 260 (4) (1991) H1365–H1378.
[16] D. Rohmer, A. Sitek, G.T. Gullberg, Reconstruction and visualization of fiber and sheet structure with regularized tensor diffusion MRI in the human heart, Lawrence Berkeley National Laboratory Publication, LBNL-60277.
[17] C.T. Stoeck, A. Kalinowska, C. von Deuster, J. Harmer, R.W. Chan, M. Niemann, R. Manka, D. Atkinson, D.E. Sosnovik, C. Mekkaoui, S. Kozerke, Dual-phase cardiac diffusion tensor imaging with strain correction, PLoS One 9 (9) (2014) 1–12.
[18] S. Uribe, T. Tangchaoren, V. Parish, I. Wolf, R. Razavi, G. Greil, T. Schaeffter, Volumetric cardiac quantification by using 3D dual-phase whole-heart MR imaging, Radiology 248 (2) (2008) 606–614.
[19] M. Usman, D. Atkinson, E. Heathfield, G. Greil, T. Schaeffter, C. Prieto, Whole left ventricular functional assessment from two minutes free breathing multi-slice CINE acquisition, Phys. Med. Biol. 60 (7) (2015) N93–N107.
[20] M. Markl, A. Frydrychowicz, S. Kozerke, M. Hope, O. Wieben, 4D flow MRI, J. Magn. Reson. Imaging 36 (5) (2012) 1015–1036.
[21] S.E. Brett, A. Guilcher, B. Clapp, P. Chowienczyk, Estimating central systolic blood pressure during oscillometric determination of blood pressure, Blood Press. Monitor. 17 (3) (2012) 132–136.
[22] P. Lamata, A. Pitcher, S. Krittian, D. Nordsletten, M.M. Bissell, T. Cassar, A.J. Barker, M. Markl, S. Neubauer, N.P. Smith, Aortic relative pressure components derived from four-dimensional flow cardiovascular magnetic resonance, Magn. Reson. Med. 72 (4) (2014) 1162–1169.
[23] F. Donati, C.A. Figueroa, N.P. Smith, P. Lamata, D.A. Nordsletten, Non-invasive pressure difference estimation from pc-mri using the work-energy equation, Medical image analysis 26 (1) (2015) 159–172.
[24] R. Chabiniok, P. Moireau, P.-F. Lesault, A. Rahmouni, J.-F. Deux, D. Chapelle, Estimation of tissue contractility from cardiac cine-MRI using a biomechanical heart model, Biomechanics and modeling in mechanobiology 11 (5) (2012) 609–630.

Please cite this article in press as: L. Asner, et al., Patient-specific modeling for left ventricular mechanics using data-driven boundary energies, Comput. Methods Appl. Mech. Engrg. (2016), http://dx.doi.org/10.1016/j.cma.2016.08.002

[25] D. Chapelle, M. Fragu, V. Mallet, P. Moireau, Fundamental principles of data assimilation underlying the verdandi library: applications to biophysical model personalization within euheart, Med. Biol. Eng. Comput. 51 (11) (2013) 1221–1233.
[26] J. Xi, P. Lamata, S. Niederer, S. Land, W. Shi, X. Zhuang, S. Ourselin, S.G. Duckett, A.K. Shetty, C.A. Rinaldi, D. Rueckert, R. Razavi, N.P. Smith, The estimation of patient-specific cardiac diastolic functions from clinical measurements, Med. Image Anal. 17 (2) (2013) 133–146.
[27] W. Shi, X. Zhuang, H. Wang, S.G. Duckett, D.V.N. Luong, C. Tobon-gomez, K. Tung, P.J. Edwards, K.S. Rhode, R.S. Razavi, S. Ourselin, D. Rueckert, A comprehensive cardiac motion estimation framework using both untagged and 3-D tagged MR images based on nonrigid registration, IEEE Trans. Med. Imaging 31 (6) (2012) 1263–1275.
[28] W. Shi, M. Jantsch, P. Aljabar, L. Pizarro, W. Bai, H. Wang, D. O'Regan, X. Zhuang, D. Rueckert, Temporal sparse free-form deformations, Med. Image Anal. 17 (7) (2013) 779–789.
[29] O. Camara, T. Mansi, M. Pop, K. Rhode, M. Sermesant, A. Young, Statistical Atlases and Computational Models of the Heart-Imaging and Modelling Challenges: 5th International Workshop, STACOM 2014, Held in Conjunction with MICCAI 2014, Boston, MA, USA, September 18, 2014, Revised Selected Papers, vol. 8896, Springer, 2015.
[30] L.A. Taber, M. Yang, W.W. Podszus, Mechanics of ventricular torsion, J. Biomech. 29 (6) (1996) 745–752.
[31] V.Y. Wang, H.I. Lam, D.B. Ennis, B.R. Cowan, A.A. Young, M.P. Nash, Cardiac active contraction parameters estimated from magnetic resonance imaging, in: Lecture Notes in Computer Science (including subseries Lecture Notes in Artificial Intelligence and Lecture Notes in Bioinformatics) 6364 LNCS, 2010, pp. 194–203.
[32] V.Y. Wang, J.A. Niestrawska, A.J. Wilson, G.B. Sands, A.A. Young, I.J. LeGrice, M.P. Nash, Image-driven constitutive modeling of myocardial fibrosis, Int. J. Comput. Methods Eng. Sci. Mech. 17 (3) (2016) 211–221.
[33] A. Nagler, C. Bertoglio, M. Gee, W. Wall, Personalization of cardiac fiber orientations from image data using the unscented Kalman filter, in: Functional Imaging and Modeling of the Heart, Springer, 2013, pp. 132–140.
[34] N. Toussaint, C.T. Stoeck, T. Schaeffter, S. Kozerke, M. Sermesant, P.G. Batchelor, In vivo human cardiac fibre architecture estimation using shape-based diffusion tensor processing, Med. Image Anal. (2013) 1243–1255.
[35] H.M. Spotnitz, Macro design, structure, and mechanics of the left ventricle, J. Thorac. Cardiovasc. Surg. 119 (5) (2000) 1053–1077.
[36] D.D. Streeter, H.M. Spotnitz, D.P. Patel, J. Ross, E.H. Sonnenblick, Fiber orientation in the canine left ventricle during diastole and systole, Circ. Res. 24 (3) (1969) 339–347.
[37] M. Hadjicharalambous, R. Chabiniok, L. Asner, E. Sammut, J. Wong, G. Carr-White, J. Lee, R. Razavi, N. Smith, D. Nordsletten, Analysis of passive cardiac constitutive laws for parameter estimation using 3D tagged MRI, Biomech. Model. Mechanobiol. 14 (4) (2015) 807–828.
[38] R.C.P. Kerckhoffs, P. Bovendeerd, F. Prinzen, K. Smits, T. Arts, Intra-and interventricular asynchrony of electromechanics in the ventricularly paced heart, J. Engrg. Math. 47 (2003) 201–216.
[39] J. Bonet, R. Wood, Nonlinear Continuum Mechanics for Finite Element Analysis, Cambridge University Press, 2008.
[40] S. Marchesseau, H. Delingette, M. Sermesant, N. Ayache, Fast parameter calibration of a cardiac electromechanical model from medical images based on the unscented transform, Biomech. Model. Mechanobiol. (2012) 1–17. URL https://hal.inria.fr/hal-00813847.
[41] E. Kayvanpour, T. Mansi, F. Sedaghat-Hamedani, A. Amr, D. Neumann, B. Georgescu, P. Seegerer, A. Kamen, J. Haas, K.S. Frese, M. Irawati, E. Wirsz, V. King, S. Buss, D. Mereles, E. Zitron, A. Keller, H.A. Katus, D. Comaniciu, B. Meder, Towards personalized cardiology: Multi-scale modeling of the failing heart, PLoS ONE 10 (2015) 1–18.
[42] F. Billet, M. Sermesant, H. Delingette, N. Ayache, Cardiac Motion Recovery and Boundary Conditions Estimation by Coupling an Electromechanical Model and Cine-MRI Data, Springer, Berlin, Heidelberg, Berlin, Heidelberg, 2009, pp. 376–385.
[43] H. Delingette, F. Billet, K.C.L. Wong, M. Sermesant, K. Rhode, M. Ginks, C.A. Rinaldi, R. Razavi, N. Ayache, Personalization of cardiac motion and contractility from images using variational data assimilation, IEEE Trans. Biomed. Eng. 59 (1) (2012) 20–24.
[44] I. Babuška, The finite element method with penalty, Math. Comp. 27 (122) (1973) 221–228.
[45] L. Asner, M. Hadjicharalambous, J. Lee, D. Nordsletten, STACOM Challenge: simulating left ventricular mechanics in the canine heart, in: Statistical Atlases and Computational Models of the Heart-Imaging and Modelling Challenges, vol. 8896, Springer, 2015, pp. 123–134.
[46] A. Gorodkov, N.B. Dobrova, J.-P. Dubernard, G.I. Kiknadze, I.A. Gatchetchiladze, V.G. Oleinikov, N.B. Kuzmina, J.L. Barat, C. Baquey, Anatomical structures determining blood flow in the heart left ventricle, J. Mater. Sci.: Mater. Med. 7 (3) (1996) 153–160.
[47] A. de Vecchi, D.A. Nordsletten, E.W. Remme, H. Bellsham-Revell, G. Greil, J.M. Simpson, R. Razavi, N.P. Smith, Inflow typology and ventricular geometry determine efficiency of filling in the hypoplastic left heart, Ann. Thorac. Surg. 94 (5) (2012) 1562–1569.
[48] M.-C. Hsu, D. Kamensky, Y. Bazilevs, M.S. Sacks, T.J. Hughes, Fluid–structure interaction analysis of bioprosthetic heart valves: significance of arterial wall deformation, Comput. Mech. 54 (4) (2014) 1055–1071.
[49] R. Van Loon, Towards computational modelling of aortic stenosis, Int. J. Numer. Methods Biomed. Eng. 26 (3–4) (2010) 405–420.
[50] H.L. Falsetti, M.S. Verani, C.-J. Chen, J.A. Cramer, Regional pressure differences in the left ventricle, Cathet. Cardiovasc. Diag. 6 (1980) 123–134.
[51] T. Ebbers, L. Wigstrom, A.F. Bolger, B. Wranne, M. Karlsson, Noninvasive measurement of relative pressure fields within the human heart, Trans. ASME 124 (June) (2002) 288–293.
[52] R.C.P. Kerckhoffs, M.L. Neal, Q. Gu, J.B. Bassingthwaighte, J.H. Omens, A.D. McCulloch, Coupling of a 3d finite element model of cardiac ventricular mechanics to lumped systems models of the systemic and pulmonic circulation, Ann. Biomed. Eng. 35 (1) (2007) 1–18.
[53] S.F. Nagueh, K.J. Middleton, H.A. Kopelen, W.A. Zoghbi, M.A. Quin, Doppler tissue imaging : A noninvasive technique for evaluation of left ventricular relaxation and estimation of filling pressures, J. Am. Coll. Cardiol. 30 (6) (1997) 1527–1533.
[54] I. Demirdžič, M. Perič, Space conservation law in finite volume calculations of fluid flow, Internat. J. Numer. Methods Fluids 8 (9) (1988) 1037–1050.
[55] V. Shamanskii, A modification of Newton's method, Ukr. Math. J. 19 (1967) 118–122.
[56] M. McCormick, D.A. Nordsletten, D. Kay, N.P. Smith, Simulating left ventricular fluid-solid mechanics through the cardiac cycle under LVAD support, J. Comput. Phys. 244 (2013) 80–96.

Please cite this article in press as: L. Asner, et al., Patient-specific modeling for left ventricular mechanics using data-driven boundary energies, Comput. Methods Appl. Mech. Engrg. (2016), http://dx.doi.org/10.1016/j.cma.2016.08.002

[57] J. Lee, A. Cookson, I. Roy, E. Kerfoot, L. Asner, G. Vigueras, T. Sochi, C. Michler, N.P. Smith, D.A. Nordsletten, Multi-physics computational modeling in CHeart, SIAM J. Sci. Comput. 38 (3) (2016) C150–C178.
[58] A. de Vecchi, A. Gomez, K. Pushparajah, T. Schaeffter, D.A. Nordsletten, J.M. Simpson, G.P. Penney, N.P. Smith, Towards a fast and efficient approach for modelling the patient-specific ventricular haemodynamics, Prog. Biophys. Mol. Biol. 116 (1) (2014) 3–10.
[59] A. Cookson, J. Lee, C. Michler, R. Chabiniok, E. Hyde, D. Nordsletten, M. Sinclair, M. Siebes, N. Smith, A novel porous mechanical framework for modelling the interaction between coronary perfusion and myocardial mechanics, J. Biomech. 45 (5) (2012) 850–855.
[60] S.A. Lambert, S.P. Näsholm, D. Nordsletten, C. Michler, L. Juge, J.-M. Serfaty, L. Bilston, B. Guzina, S. Holm, R. Sinkus, Bridging three orders of magnitude: multiple scattered waves sense fractal microscopic structures via dispersion, Phys. Rev. Lett. 115 (9) (2015) 094301.
[61] G. Vigueras, I. Roy, A. Cookson, J. Lee, N. Smith, D. Nordsletten, Toward GPGPU accelerated human electromechanical cardiac simulations, Int. J. Numer. Methods Biomed. Eng. 30 (1) (2014) 117–134.
[62] D. Peressutti, W. Bai, T. Jackson, M. Sohal, A. Rinaldi, D. Rueckert, A. King, Prospective identification of CRT super responders using a motion atlas and random projection ensemble learning, in: Medical Image Computing and Computer-Assisted Intervention–MICCAI 2015, Springer, 2015, pp. 493–500.
[63] K. Russell, M. Eriksen, L. Aaberge, N. Wilhelmsen, H. Skulstad, E.W. Remme, K.H. Haugaa, A. Opdahl, J.G. Fjeld, O. Gjesdal, T. Edvardsen, O.A. Smiseth, A novel clinical method for quantification of regional left ventricular pressurestrain loop area: A non-invasive index of myocardial work, Eur. Heart J. 33 (6) (2012) 724–733.
[64] S. Göktepe, S. Acharya, J. Wong, E. Kuhl, Computational modeling of passive myocardium, Int. J. Numer. Methods Biomed. Eng. 27 (1) (2011) 1–12.
[65] C. Stevens, E. Remme, I. LeGrice, P. Hunter, Ventricular mechanics in diastole: Material parameter sensitivity, J. Biomech. 36 (November 2002) (2003) 737–748.
[66] M. Hadjicharalambous, J. Lee, N.P. Smith, D.A. Nordsletten, A displacement-based finite element formulation for incompressible and nearly-incompressible cardiac mechanics, Comput. Methods Appl. Mech. Engrg. 274 (2014) 213–236.
[67] H.M. Wang, X.Y. Luo, H. Gao, R.W. Ogden, B.E. Griffith, C. Berry, T.J. Wang, A modified Holzapfel-Ogden law for a residually stressed finite strain model of the human left ventricle in diastole, Biomech. Model. Mechanobiol. 13 (2014) 99–113.
[68] J.H. Omens, T.P. Usyk, Z. Li, A.D. McCulloch, Muscle LIM protein deficiency leads to alterations in passive ventricular mechanics, Am. J. Physiol. Heart Circ. Physiol. 282 (2002) H680–H687.
[69] S. Pezzuto, D. Ambrosi, Active contraction of the cardiac ventricle and distortion of the microstructural architecture, International journal for numerical methods in biomedical engineering 30 (12) (2014) 1578–1596.
[70] A. Quarteroni, A. Valli, Numerical Approximation of Partial Differential Equations, vol. 23, Springer Science & Business Media, 2008.

Please cite this article in press as: L. Asner, et al., Patient-specific modeling for left ventricular mechanics using data-driven boundary energies, Comput. Methods Appl. Mech. Engrg. (2016), http://dx.doi.org/10.1016/j.cma.2016.08.002